Nonlinear Dynamics (2026) 114:1046
https://doi.org/10.1007/s11071-026-12884-z

RESEARCH

Energy-based control of a nonlinear hybrid-propulsion aircraft system

Danilo Ciliberti[1] · Agostino De Marco[1]

Received: 29 March 2026 / Revised: 2 July 2026 / Accepted: 18 July 2026

Abstract
This paper presents the integration of an energy-based control system, a hybrid-electric nonlinear aircraft model, and differentiable flight-envelope protection functions for simulation-based design workflows. A fully nonlinear 3-DoF aero-propulsive model for a propeller-driven, hybrid-electric, regional transport aircraft is presented and coupled with the Total Energy Control System (TECS). The proposed formulation explicitly addresses features that are critical in realistic hybrid-electric flight simulation, including variable-mass, power lapse, flight-envelope protection implemented through smooth blending functions, and Control Authority Allocation (CAA) in saturated operating conditions. The resulting framework supports controlled mission simulation over a wide range of operating scenarios while preserving a continuous implementation suitable for Functional Mock-up Interface (FMI) compliant workflows. Results show effective airspeed and flight-path tracking, energy-consistent climb and descent behavior, and safe operation under different mission phases. The study demonstrates that TECS can be extended from conventional and linearized models to fully nonlinear hybrid-propulsion configurations, providing a generalizable basis for advanced nonlinear aircraft control and verification-oriented simulation.

Keywords Flight dynamics modeling · nonlinear control · Hybrid-electric propulsion · Flight-envelope protection

1 Introduction

Hybrid-Electric Regional Aircraft (HERA) constitute a particularly challenging class of aerospace systems from the viewpoint of nonlinear dynamics and control. Their behavior is governed by aerodynamic forces and moments that depend nonlinearly on the aircraft state and operating condition, together with strongly coupled aero-propulsive interactions, propulsion constraints, and mission-dependent energy-management requirements. Accurate controlled mission simulation therefore requires physically-grounded nonlinear aero-propulsive models together with longitudinal control architectures capable of coordinating airspeed and flight-path tracking while accounting for variable-mass effects, actuator saturation, and envelope-protection requirements.

The aviation industry is undergoing a significant transformation toward climate-neutral solutions, with HERA emerging as a promising pathway for short-range air mobility.[1] However, the development of such aircraft presents unprecedented challenges due to their inherent complexity, which significantly exceeds that of conventional configurations. For instance, hybrid-electric propulsion systems can involve up to 2.6 times more parameters and 7 times more parametrization combinations compared to conventional systems,[2] thus necessitating novel approaches to aircraft development. The ODE4HERA project has addressed these challenges by developing an Open Digital Platform (ODP) that combines different technologies to accelerate the development of hybrid-electric regional aircraft configurations, targeting a 50% improvement in cost-effectiveness and a 50% reduction in lead time with respect to 2020 state-of-the-art references.

Within this context, the flight-mechanics model is a key enabling technology, since it provides the basis for simulating and analyzing aircraft performance over different flight

✉ Agostino De Marco
agostino.demarco@unina.it

Danilo Ciliberti
danilo.ciliberti@unina.it

1 Department of Industrial Engineering (DII), Università degli Studi di Napoli Federico II, Via Claudio, 21, 80125 Naples, Italy

[1] HERA, Hybrid-Electric Regional Aircraft, is a research project co-funded by the European Union under Grant Agreement no. 101102007. https://project-hera.eu.

[2] Data from the ODE4HERA project's grant agreement. ODE4HERA, Open Digital Environment for Hybrid-Electric Regional Architectures, is a research project co-funded by the European Union under Grant Agreement no. 101140510. https://www.ode4hera.eu.

Published online: 14 August 2026

conditions and mission profiles. For hybrid-electric configurations, such a model must capture not only the conventional aircraft dynamics, but also the effects of hybrid propulsion on mission management, energy usage, and flight control. Engineering flight simulations therefore play a central role in the ODE4HERA framework as part of the behavioral modeling and integration of HERA technologies within verification and validation procedures. In particular, controlled flight simulations are essential because they enable rapid and automated assessment of aircraft behavior in response to assigned mission profiles, which is critical for the design and optimization of hybrid-electric platforms.

The traditional approach to flight control has long relied on the assumption of approximately decoupled aircraft dynamics, with each control axis treated independently according to Single-Input-Single-Output (SISO) control architectures [1]. This viewpoint led to separate feedback loops for longitudinal and lateral-directional motion, each associated with a specific set of actuators and controlled variables. A major conceptual shift occurred when aircraft motion began to be recognized as an intrinsically coupled Multiple-Input-Multiple-Output (MIMO) system. In wings-level flight, this evolution culminated in the Total Energy Control System (TECS), introduced by Lambregts in the early 1980s [2–4], which reformulated longitudinal flight control on the basis of energy principles. By explicitly controlling the total energy state and the balance between its kinetic and potential components, TECS provides an effective framework for the coordinated regulation of flight path and airspeed. Similar developments in lateral-directional control led to the Total Heading Control System (THCS) [5], although energy-based methods have found their most natural application in longitudinal control, where potential and kinetic energy exchanges dominate the dynamics.

The separated altitude and airspeed controllers of conventional longitudinal flight-control systems may lead to undesirable coupling effects and suboptimal energy management. TECS offers a more coherent solution, since it directly addresses the exchange and distribution of aircraft energy. Much of the classical TECS literature has focused on conventional commercial jet transports and on analysis and tuning based on linearized representations of their dynamics, as reported in [6, 7]. A distinguishing feature of TECS is its substantial independence from the specific aircraft configuration, owing to its energy-based formulation [2]. In contrast to multiple-SISO architectures, which often require extensive redesign and retuning when transferred across platforms, the core TECS algorithm remains largely invariant and has been successfully implemented for a broad range of aircraft types [7–12]. Moreover, the energy-based formulation naturally accommodates important nonlinear effects, such as thrust lapse with altitude and speed, as well as variations in aerodynamic characteristics across the flight envelope.

These properties make TECS especially attractive for hybrid-propulsion aircraft, yet its application in that setting is far from straightforward. Realistic aero-propulsive models of hybrid-electric aircraft contain adaptive and mode-dependent elements, actuator saturations, and operational constraints that complicate both the control design and the numerical implementation. In addition, regional transport requirements introduce different mission profiles and performance targets, including the coordinated management of energy drawn from electric and conventional power sources over a wide range of flight conditions. As a consequence, extending TECS from conventional aircraft applications to hybrid-electric regional aircraft requires not only a suitable nonlinear flight-dynamics model, but also a control implementation capable of handling envelope protection and transition logic without compromising simulation robustness.

The objective of this research is therefore to demonstrate an advanced TECS application to a fully nonlinear model of a hybrid-electric, propeller-driven aircraft. More specifically, the paper addresses: (i) the implementation challenges associated with the adaptive elements commonly found in realistic aero-propulsive models; (ii) the development of a comprehensive flight-envelope protection system that leverages the TECS energy-based framework; and (iii) the implementation of all control logic through continuous functions, so that the Flight Mechanics and Flight Control System modules are compliant with Functional Mockup Interface[3] (FMI) version 2.0. This last aspect is particularly relevant to the integrated verification and validation phase of a solution-neutral ODP.

Accordingly, the contribution of the paper lies in the integration of nonlinear flight-dynamics modeling, aero-propulsive representation, and energy-based control into a single simulation-oriented framework for hybrid-electric regional aircraft. The emphasis is not merely on implementing TECS on a new platform, but on showing how a nonlinear model and a continuous-control formulation can be combined to support controlled mission simulations, safe flight-envelope operation, and future integration as a Functional Mock-up Unit (FMU) within the ODE4HERA digital environment.

The remainder of this article is organized as follows. Section 2 presents the nonlinear 3-DoF flight-dynamics model, listing the equations implemented in the simulation framework. Section 3 revisits the theoretical foundations of the Total Energy Control System, deriving the thrust and elevator control laws from energy principles and describing the TECS core algorithm structure, including gain scheduling of the aircraft-dependent inner loops. Section 4 introduces examples of mission simulation, demonstrating the flight-envelope

[3] Functional Mock-up Interface is a Modelica Association Project. https://fmi-standard.org/.

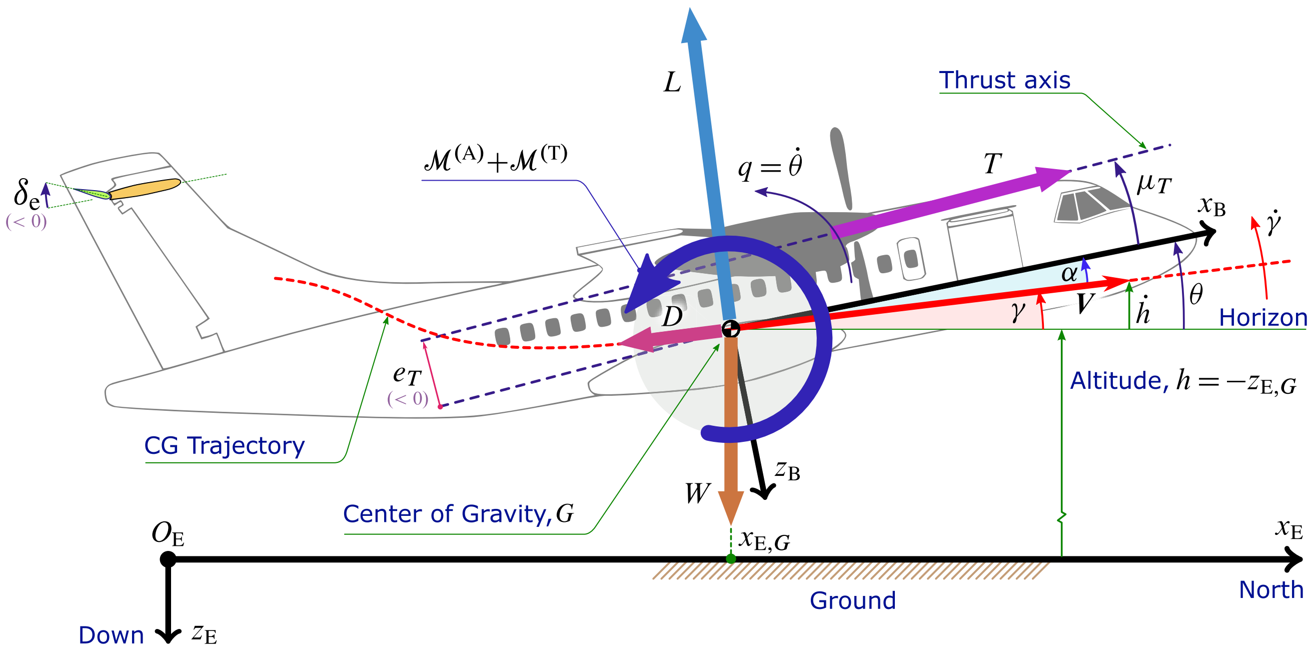

Fig. 1 Earth-based NED frame $\mathcal{F}_\mathrm{E} = \{O_\mathrm{E}; x_\mathrm{E}, y_\mathrm{E}, z_\mathrm{E}\}$ and aircraft body-fixed frame $\mathcal{F}_\mathrm{B} = \{G; x_\mathrm{B}, y_\mathrm{B}, z_\mathrm{B}\}$ in wings-level flight (axes y_E and y_B normal to the page). Planar trajectory and velocity vector $\boldsymbol{V}$ of aircraft gravity center G with respect to the inertial observer. Standard definitions of altitude $h = -z_{\mathrm{E},G}$, aircraft second Euler angle θ (elevation angle), and flight path angle γ. Aerodynamic angle α, elevator angle deflection δ_e, and pitch rate q

protection logic adopted to ensure safe operation under different mission profiles. Section 5 evaluates the robustness of the flight-envelope protection system with Monte Carlo simulations and presents two mission trajectories in the altitude-airspeed plane. Finally, Sect. 6 summarizes the main findings and discusses the future integration of the proposed model as a Functional Mock-up Unit within the ODE4HERA Open Digital Platform.

2 Hybrid-electric aircraft 3-DoF, variable-mass flight dynamics model

The general six-degrees-of-freedom (6-DoF) atmospheric motion of a rigid airplane is governed by a set of nonlinear ordinary differential equations [13–16]. The system of equations can be expressed in a suitable explicit form and implemented in a simulation framework of choice, by adopting a properly engineered aero-propulsive model. The 3-DoF model of the aircraft wings-level flight is a particular case of the general 6-DoF formulation. The derivation of such systems assumes a clear identification of a ground-based and of an aircraft-fixed frame of reference. The former is treated as an inertial frame, neglecting the effects of the Earth's rotation, which is a good approximation when describing the confined motion of airplanes in the lower regions of the atmosphere. This approximation is acceptable for subsonic flight and fits the mission-oriented studies for the hybrid-electric regional transport aircraft considered in this research. The two main reference frames are shown in Fig. 1 for the 3-DoF case. In the 3-DoF case, a so-called 'longitudinal-symmetric flight' condition occurs, that is: (i) the aircraft external shape is symmetric with respect to the longitudinal plane $x_\mathrm{B} y_\mathrm{B}$, (ii) the relative wind $-\boldsymbol{V}$ is always in the plane $x_\mathrm{B} z_\mathrm{B}$ (with a zero wind gust field and zero y_B-component of $\boldsymbol{V}$), (iii) the resultant thrust is always in this symmetry plane, (iv) the flight is constantly wings level, (v) lateral-directional external forces and moments are always zero.

The conditions for a longitudinal-symmetric motion are assured by assuming that the pilot is not acting on controls in ways that cause asymmetry in the external actions, both aerodynamic and propulsive: ailerons and rudder are kept in a neutral position and no asymmetries in thrust delivery occur. These conditions imply that the aircraft maintains its symmetry plane constantly vertical, and that the yaw angle is kept constant for the entire duration of the motion. In the present study, the pilot is assumed to act only on the elevator and throttle. The elevator is used to control the pitch angle θ, while the throttle is used to control the thrust magnitude T.

2.1 Longitudinal flight dynamics equations

According to Fig. 1, the 3-DoF flight dynamics equations in the aircraft body-fixed frame $\mathcal{F}_\mathrm{B}$ are formulated as follows:

$$\begin{cases} \dot{u} = -g\sin\theta + \dfrac{1}{m}\left(F_{x_\mathrm{B}}^{(\mathrm{A})} + F_{x_\mathrm{B}}^{(\mathrm{T})}\right) - q\,w \\ \dot{w} = g\cos\theta + \dfrac{1}{m}\left(F_{z_\mathrm{B}}^{(\mathrm{A})} + F_{z_\mathrm{B}}^{(\mathrm{T})}\right) + q\,u \\ \dot{q} = \dfrac{1}{I_{yy}}\left(\mathcal{M}^{(\mathrm{A})} + \mathcal{M}^{(\mathrm{T})}\right) \end{cases} \tag{1}$$

The instantaneous resultant aerodynamic force $\boldsymbol{F}^{(\mathrm{A})}$, when projected onto $\mathcal{F}_\mathrm{B}$, is commonly expressed as follows:

$$\begin{aligned} F_{x_\mathrm{B}}^{(\mathrm{A})} &= -D\cos\alpha + L\sin\alpha, \\ F_{z_\mathrm{B}}^{(\mathrm{A})} &= -D\sin\alpha - L\cos\alpha \end{aligned} \tag{2}$$

that is, in terms of drag and lift forces, L and D. The latter are formulated in terms of their aerodynamic coefficients according to the conventional formulas:

$$D = \frac{1}{2}\rho V^2 S\,C_D, \qquad L = \frac{1}{2}\rho V^2 S\,C_L \tag{3}$$

where the external air density ρ is a known function of the flight altitude $h \equiv -z_{\mathrm{E},G}$ (along with other gas properties, such as the sound speed a) [17], S is a constant reference area, and coefficients (C_D, C_L) are modeled as functions of aircraft state variables and external inputs. According to Fig. 1, the state variables (u, w) are expressed in terms of α as follows:

$$u = V\cos\alpha, \qquad w = V\sin\alpha \tag{4}$$

with $V = \sqrt{u^2 + w^2}$. Consequently, the instantaneous angle of attack is given by $\alpha = \tan^{-1}\left(w/u\right)$.

The resultant thrust force $\boldsymbol{F}^{(\mathrm{T})}$ is a vector of magnitude T, of components:

$$F_{x_\mathrm{B}}^{(\mathrm{T})} = T\cos\mu_\mathrm{T}, \qquad F_{z_\mathrm{B}}^{(\mathrm{T})} = -T\sin\mu_\mathrm{T} \tag{5}$$

in the body-fixed frame $\mathcal{F}_\mathrm{B}$.

The moment of inertia I_{yy} is a varying quantity in a variable-mass model, and for the specific application presented here, its time law is determined directly from the total mass time history $m(t)$. In longitudinal-symmetric flight - with a thrust line in the aircraft symmetry plane - the only nonzero component in frame $\mathcal{F}_\mathrm{B}$ of the instantaneous resultant external barycentric moment vector is the pitch moment $\mathcal{M}$, which is commonly expressed as the sum:

$$\mathcal{M} = \mathcal{M}^{(\mathrm{A})} + \mathcal{M}^{(\mathrm{T})} \tag{6}$$

that is, the aerodynamic pitching moment $\mathcal{M}^{(\mathrm{A})}$ and the pitching moment due to thrust $\mathcal{M}^{(\mathrm{T})}$. As for the aerodynamic force coefficients, for the present study the aerodynamic pitching moment coefficient $C_\mathcal{M}$ - defined such that

$$\mathcal{M}^{(\mathrm{A})} = \frac{1}{2}\rho_\infty V^2 S\,\bar{c}\,C_\mathcal{M} \tag{7}$$

where $\bar{c}$ is a reference length known from the airplane's geometry, usually the wing mean aerodynamic chord - is available in tabulated form as a nonlinear function of the angle of attack α and elevator deflection angle δ_e. The pitching moment due to thrust $\mathcal{M}^{(\mathrm{T})}$ is given by the direct action of the thrust vector:

$$\mathcal{M}^{(\mathrm{T})} = T\,e_\mathrm{T} \tag{8}$$

where the eccentricity e_T is a known parameter, positive when the thrust line is located beneath the center of gravity ($e_\mathrm{T} < 0$ as shown in Fig. 1).

The equations describing the 3-DoF airplane's kinematics, i. e. CG's trajectory in frame $\mathcal{F}_\mathrm{E}$ and rigid-body attitude, are formulated as follows:

$$\begin{cases} \dot{x}_{\mathrm{E},G} = \sqrt{u^2 + w^2}\;\cos\left(\theta - \tan^{-1}\dfrac{w}{u}\right) \\ \dot{z}_{\mathrm{E},G} = -\sqrt{u^2 + w^2}\;\sin\left(\theta - \tan^{-1}\dfrac{w}{u}\right) \\ \dot{\theta} = q \end{cases} \tag{9}$$

The system of equations (9) coupled with (1) form the full set of nonlinear differential equations governing the 3-DoF rigid-body dynamics of atmospheric flight. They are explicitly expressed once the fuel consumption model (i.e. the fuel flow $\dot{m}$) is defined and the aerodynamic as well as the propulsive external forces and moments are completely modeled as functions of the 7-component state vector $\boldsymbol{x}$:

$$\boldsymbol{x} = \left[\,u,\, w,\, q,\, x_{\mathrm{E},G},\, z_{\mathrm{E},G},\, \theta,\, m\,\right]^\mathrm{T} \tag{10}$$

and of the external inputs grouped as components of an input vector $\boldsymbol{u}$:

$$\boldsymbol{u} = \left[\,\delta_\mathrm{e},\, \delta_\mathrm{T}\,\right]^\mathrm{T} \tag{11}$$

collecting the elevator deflection and throttle setting.

2.2 Hybrid-electric propulsive model

The instantaneous total mass m is the last state variable listed in (10). It is a function of the fuel mass flow rate and of the throttle setting time profile. For the specific case of a hybrid-electric regional transport aircraft that uses fuel cell

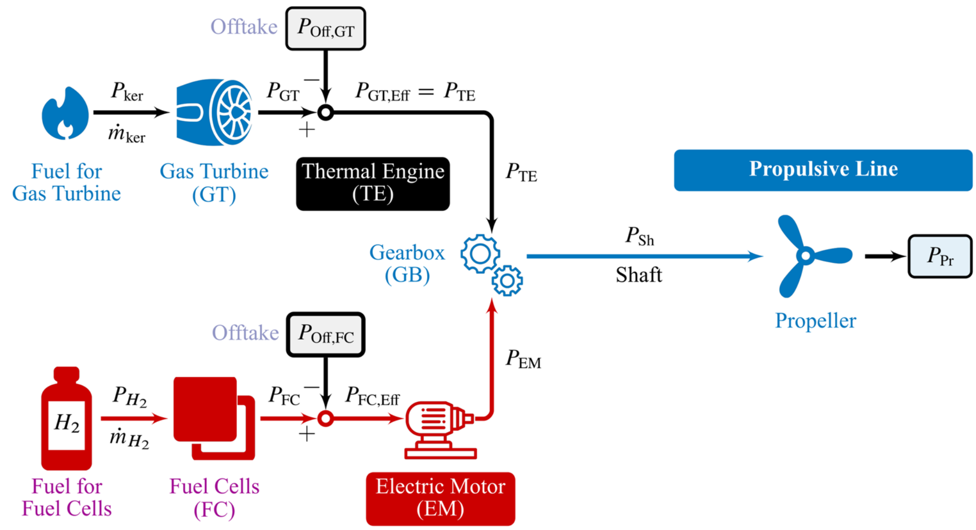

Fig. 2 Simplified hybridization scheme of a single propeller hybrid-electric system. This model generalizes for a multiple propeller configuration, by assuming that each propeller is powered by its own thermal engine (TE) coupled with its own electric motor (EM)

technology, the total mass is the sum $m(t) = m_0 + m_{\mathrm{ker}}(t) + m_{H_2}(t)$, with the constant m_0 being the known zero-fuel mass of the aircraft, and with m_{ker} and m_{H_2} being the instantaneous masses of the kerosene and of the hydrogen fuel, respectively. The initial values $m_{\mathrm{ker}}(0)$ and $m_{H_2}(0)$, at time $t = 0$, are known from the designated fuel load, and the propagation equation for m is simply given by the following:

$$\dot{m} = -\dot{m}_{\mathrm{ker}} - \dot{m}_{H_2} \tag{12}$$

where $\dot{m}_{\mathrm{ker}}$ and $\dot{m}_{H_2}$ are the mass flow rates, commonly expressed as tabulated functions of flight conditions (altitude h and airspeed V, or flight Mach number M), as well as of throttle setting δ_{T}, and of the hybridization factor Φ.

Figure 2 presents the simplified scheme of a single hybrid-electric propulsion unit. Defining η_{GB} as the gearbox efficiency, the instantaneous shaft power delivered to the propeller is given by $P_{\mathrm{sh}} = \eta_{\mathrm{GB}}\big(P_{\mathrm{TE}} + P_{\mathrm{EM}}\big)$, where P_{TE} and P_{EM} are the instantaneous powers delivered at their shafts by the thermal engine and by the electric motor, respectively. Hence, the throttle setting δ_{T} is defined as the ratio of the instantaneous cumulated power $P_{\mathrm{sh}}/\eta_{\mathrm{GB}}$ to the maximum available shaft power $P_{\mathrm{TE,max}} + P_{\mathrm{EM,max}}$ in the same flight condition:

$$\begin{aligned}\delta_{\mathrm{T}} &= \frac{P_{\mathrm{TE}} + P_{\mathrm{EM}}}{P_{\mathrm{TE,max}} + P_{\mathrm{EM,max}}}\\ &= \frac{P_{\mathrm{sh}}/\eta_{\mathrm{GB}}}{P_{\mathrm{TE,max}} + P_{\mathrm{EM,max}}}\end{aligned} \tag{13}$$

This scalar, that varies between 0 and 1, represents the main input to the propulsion system, and is used to control the instantaneous thrust delivered by the propellers, being the main source of external force to drive a given flight task.

The engine deck of the hybrid-electric power plant modelled in this study was adapted from [18]. The performance characteristics of the propulsion system are given as tabular data of powers, fuel rates, and pollutant emissions of the main components in the deck: gas turbine (thermal engine) and electric motor. The thrust has been modeled assuming that each propeller behaves as an actuator disk [19] with a maximum efficiency of 85%. For a given throttle level, the thrust is a nonlinear function of airspeed and altitude.

A further important parameter is the hybridization factor Φ, which represents the relative contribution of the electric motor to the total power delivered by the combined thermal engine-electric motor system. This factor is defined as the ratio:

$$\Phi = \frac{P_{\mathrm{EM}}}{P_{\mathrm{TE}} + P_{\mathrm{EM}}} \tag{14}$$

A value of $\Phi = 0$ corresponds to a conventional propulsion mode driven entirely by the thermal engine. When Φ approaches 1, the system transitions to a full-electric mode where the electric motor delivers the majority of the power. The hybridization factor is a key parameter for modeling the propulsion system, as it directly influences the fuel consumption, the emissions, the delivered shaft power, and hence the thrust. In general, it is a function of throttle setting δ_{T}, flight Mach number M, and altitude h.

3 The total energy control system (TECS)

As shown also by other works [2, 6, 7] dealing with fixed-wing aircraft configurations, the TECS is a MIMO energy-based navigation control strategy that is capable to provide all vertical flight path and airspeed control mode functions. TECS is able to achieve an effective control on flight path and speed setpoints separately, still acting on throttle and elevator, but overcoming the limitations of SISO control systems that manage altitude and speed independently. This is accomplished by regulating the aircraft total energy during the commanded mission, and facilitating energy transfer between kinetic and potential gravitational forms. In this work, TECS is therefore adopted as a proven baseline control strategy, and the focus is placed on its integration with a nonlinear hybrid-propulsion model and envelope-protection logic rather than on re-evaluating its performance against classical longitudinal control laws. The updated TECS model [4], the inner-loops controller, and their implementation are summarized in the present section.

Based on the well-known theory of transport aircraft performance [14, 20], where the vehicle is modeled as a point mass, with the further assumption of a slowly varying mass, the total energy $\mathcal{E}$ of an aircraft in flight can be expressed as the sum of its gravitational potential and kinetic energy:

$$\mathcal{E} = mgh + \frac{1}{2} m V^2 \tag{15}$$

Therefore, the specific energy rate $\dot{E} = \dot{\mathcal{E}}/(mgV)$ can be expressed as:

$$\dot{E} \equiv \frac{\dot{\mathcal{E}}}{mgV} = \frac{\dot{h}}{V} + \frac{\dot{V}}{g} \tag{16}$$

From the Newton's second law applied to the airplane modeled as a point mass [20], projected along the instantaneous tangent x_A to the flight trajectory (see Fig. 1), assuming $\theta \approx \gamma$, for small values of the flight path angle, it follows that $\dot{h}/V \approx \gamma$ and that the instantaneous 'excess thrust over drag' is directly proportional to the specific energy rate:

$$T - D = mg\left(\gamma + \frac{\dot{V}}{g}\right) = mg\dot{E} \tag{17}$$

The above expression states that altering the thrust command T will alter the specific energy rate $\dot{E}$, hence the airplane's total energy.

For a level flight along a horizontal trajectory ($\gamma = 0$), at constant speed ($\dot{V} = 0$), the thrust is trimmed against drag ($T - D = 0$), and a thrust variation ΔT with respect to its equilibrium value is expressed as follows:

$$\Delta T = mg\left(\varepsilon_\gamma + \frac{\varepsilon_{\dot{V}}}{g}\right) \propto \varepsilon_{\dot{E}} \tag{18}$$

where $\varepsilon_\gamma = \gamma - \gamma_\mathrm{c}$, $\varepsilon_{\dot{V}} = \dot{V} - \dot{V}_\mathrm{c}$, and $\varepsilon_{\dot{E}} = \dot{E} - \dot{E}_\mathrm{c}$ are the errors in γ, $\dot{V}$, and $\dot{E}$, respectively, on the 'commanded' values $(\cdot)_\mathrm{c}$. Equation (18), confirms that a change in thrust causes a combined change of the flight path angle and of the acceleration along the trajectory - a fact that brought to the idea of using the engine throttle as a control input to regulate the total energy of the airplane, as in a reservoir analogy [3]. This principle is the basis of the TECS control strategy, which can be generalized to direct a mission by commanding changes in flight path angle and speed, or in altitude and Mach number, or else in any other pair of energy-related variables.

The TECS core algorithm receives the commanded signals γ_c and $(\dot{V}/g)_\mathrm{c}$, transforming them into commanded thrust and elevation angle signals, T_c and θ_c, respectively. Altitude-and-Airspeed hold mode is the most common mode of operation for TECS technology implemented on fixed-wing aircraft and will be demonstrated in the examples shown in the next sections.

A TECS Core block is shown in Fig. 3, providing more details on what is usually called the 'outer loop' of the overall TECS control scheme. In the TECS Core algorithm structure of Fig. 3, besides the specific energy rate $\dot{E}$, the specific energy distribution rate

$$\dot{L} = \frac{\dot{V}}{g} - \gamma \tag{19}$$

is also used as an observed variable. The quantity $\dot{L}$, also known as the Lagrangian, is a measure of how the total energy is distributed between potential and kinetic forms, and is used to generate the elevator command δ_e to control the flight path angle γ and hence the altitude h of the airplane. The TECS Core treats the errors ε_γ and $\varepsilon_{\dot{V}}$ as inputs, and generates the thrust command T_c and the elevation command θ_c as outputs. The latter two quantities are then fed to the Inner-loops block which, in turn, generates the actual control commands δ_T and δ_e for the throttle and elevator actuators, respectively. The chosen control algorithm structure for developing coordinated thrust and elevator commands employs proportional and integral control feedback. However, only $\dot{E}$ and $\dot{L}$ feedbacks are used for the proportional terms instead of the error signals to prevent the creation of unwanted zeros in the system transfer functions, which would lead to undesirable overshoot in the command response.

A simple Proportional-Integral control is then formulated to relate the desired changes in energy rate to thrust (T_c) and thrust setting (δ_T) commands, in the form of the following transfer laws:

$$T_\mathrm{c} = W\left(K_\mathrm{TP} + \frac{K_\mathrm{TI}}{s}\right)\varepsilon_{\dot{E}}$$
$$\implies \delta_\mathrm{T} = \left(K_{\delta_\mathrm{T}\mathrm{P}} + \frac{K_{\delta_\mathrm{T}\mathrm{I}}}{s}\right) T_\mathrm{c} \tag{20}$$

where K_TP and K_TI are respectively the proportional and the integral gains of the TECS thrust command. According to Fig. 3 (Outer-loops, TECS Core), these gains do not depend on the aircraft particular model.

On the contrary, the scheduled PI controller's gains $K_{\delta_\mathrm{T}\mathrm{P}}$ and $K_{\delta_\mathrm{T}\mathrm{I}}$ (Fig. 3, Inner-loops, Throttle controller) are pro-

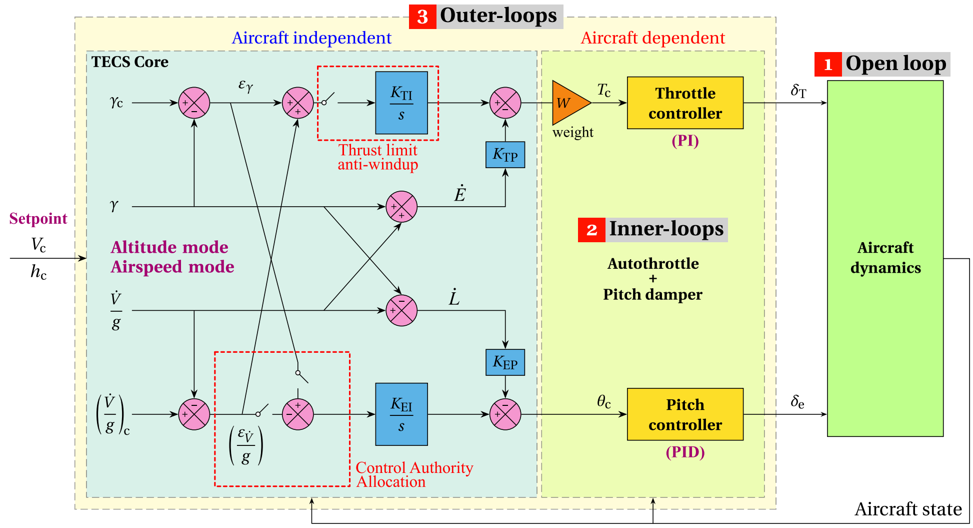

Fig. 3 The TECS Core and Inner-loops blocks forming the Outer-loops of the TECS scheme. The TECS drives the Open-loop nonlinear plant model, generating the control commands δ_T and δ_e for the throttle and elevator actuators, respectively

vided by interpolating functions of airspeed and altitude over sets of fine-tuned values obtained for a dense grid of operating points within the performance envelope of the specific airplane under study. In this scenario, the TECS integral control (K_{TI}/s) is essential for adjusting T_c to any desired condition and drive the error $\varepsilon_{\dot{E}}$ to zero. Also, such loop is open when thrust saturates and the error signal keeps growing, avoiding the windup of the integral controller.

Regarding the other input option to the open-loop plant model, i.e. the commanded elevator δ_e deflection, it is well known that elevator control is able to maintain a desired energy level with good approximation [2, 3]. This allows the pilot to exchange potential energy for kinetic energy and vice versa using this aerodynamic surface, without significant short-term energy loss. Therefore, the elevator can be used for energy distribution control. A second Proportional-Integral control law can be applied to convert errors in the desired energy distribution rate $\varepsilon_{\dot{L}}$ into attitude angles and, consequently, into elevator angle commands:

$$\theta_c = \left(K_{EP} + \frac{K_{EI}}{s}\right)\varepsilon_{\dot{L}} \implies \delta_e = \left(K_{\theta P} + \frac{K_{\theta I}}{s} + K_{\theta D}\, s\right)\theta_c \tag{21}$$

where K_{EP} and K_{EI} are respectively the proportional and the integral TECS core gains of the commanded attitude angle θ_c. Again, according to Fig. 3 (Inner-loops, Pitch controller), the functions $K_{\theta P}$, $K_{\theta I}$, $K_{\theta D}$ are implemented as gain-scheduled PID laws whose gains vary with airspeed and altitude. The gain lookup tables are generated off line in MATLAB by tuning the SISO inner loops on a grid of altitude/airspeed operating points, so as to achieve a consistent target response, and subsequently imported into the Simulink implementation. Final gains are validated by inspection of the closed loop time histories before deployment.

The TECS core feedback gains K_{TI}, K_{TP}, K_{EI}, and K_{EP} used in developing the thrust and elevator commands, are designed to produce identical dynamics for energy rate error $\varepsilon_{\dot{E}}$ and energy distribution rate error $\varepsilon_{\dot{L}}$, whether for a flight path angle command or a longitudinal acceleration command. At this scope, the identical dynamics are achieved by posing $K_{TI} = K_{EI}$ and $K_{TP} = K_{EP}$. However, tuning of these gains is predominantly heuristic. This can be a limitation for strictly optimal performance.

The MIMO control law enables accurate coordination of thrust and elevator to achieve decoupled command responses. Consequently, a flight path angle command will not cause significant speed deviation and vice versa. Another perspective on command response decoupling is that for a flight path angle or acceleration command, the dynamic response of $\varepsilon_{\dot{E}}$ and $\varepsilon_{\dot{L}}$ must be identical; otherwise, energy is added to or subtracted from the variable intended to remain constant.

4 Mission management simulations

The applications presented here consider a reference aircraft design similar to the Ultra Efficient Regional Aircraft (UERA) under development in the HERA project. See Table 1 and Fig. 4 showing the main data of the twin-propeller regional transport platform and of the parallel hybrid-electric power plant. The inherent coupling between the airframe and propulsion system introduces significant nonlinearities in the aerodynamic and thrust models, posing a significant challenge for the mission simulation and control. Appendix A presents the details of a nonlinear aerodynamic model for the hybrid-electric aircraft considered in this study. Appendix B illustrates the propulsive model, where the optimal hybridiza-

Table 1 Main aircraft data

Geometric and inertia properties	
Length, L	27.20 m
Wing span, b	30.15 m
Wing surface, S	65.60 m^2
Wing Aspect Ratio,	13.85
Maximum Take-Off Mass, MTOM	27600 kg
Moment of inertia, I_{yy}	$4.15 \cdot 10^5$ kg^{2}m^2
Power plant properties (static, sea level)	
Electric motor power (per unit), P_{EM}	765 kW
Thermal engine power (per unit), P_{TE}	2100 kW
Total shaft power (2 units), P_{sh}	5600 kW

tion strategy has been previously fixed by the propulsion specialists. The online energy management of the power plant is out of the scope of this work. Appendix C shows some examples of the gains of the inner-loops controllers scheduled against airspeed and altitude.

A typical TECS-based autopilot architecture involves multiple control modes. In our application the TECS works in altitude-and-airspeed hold mode. Mission management is performed by another outer loop, called Normalized Commands Generator, transforming a sequence of airspeed-altitude combinations into TECS input. As shown in Fig. 5, commanded signals of airspeed V_{c} and altitude h_{c} are compared to the actual values V and h, respectively. The airspeed and altitude error signals, ε_V and ε_h respectively, are transformed into normalized acceleration command $(\dot{V}/g)_{\mathrm{c}}$ and flight path angle command γ_{c}, respectively:

$$\left(\frac{\dot{V}}{g}\right)_{\mathrm{c}} = K\,\varepsilon_V\,, \qquad \gamma_{\mathrm{c}} = K\,\frac{\varepsilon_h}{V} \tag{22}$$

where the proportional gain K is a constant found by trial and error, such that the accurate tracking of airspeed and altitude for a small commanded step of the initial values is reasonably fast without excessive overshoot or divergence of the responses [21, 22].

In the following, a selected set of simulation examples is presented, starting from the demonstration of variables decoupling in Sec. 4.1. Then, two demanding climbs from low to high altitude are shown: one at constant airspeed in Sec. 4.2 and the other tracking the maximum vertical speed in Sec. 4.3. A similar mission management with the opposite objective is demonstrated in Sec. 4.4, where a descent from high to low altitude at constant airspeed is requested. Finally, a typical mission profile is presented in Sec. 4.5, where a realistic sequence of airspeed and altitude setpoints is assigned. Each of the presented test cases introduced new challenges that required additional modules in the outer loop and in the TECS core to guarantee a safe flight.

4.1 Tuned TECS for airspeed and altitude setpoint decoupling

This simple test case serves to verify the implementation of the TECS core algorithm. Starting from trimmed conditions at a given airspeed and altitude, a small commanded variation in airspeed shall not alter the steady-state altitude, and viceversa. This effectively demonstrates the altitude and speed decoupling. The results of two separate simulations are shown in Fig. 6, both with a duration time of two minutes. The plots show that the system moves to another steady state, although it achieves the intended target much faster. It is apparent that the alternatively assigned steps in airspeed and altitude are accurately tracked, with elevator δ_{e} and throttle δ_{T} commands activated at the same time. Both inputs have the same error dynamics, represented by the specific energy rates $\dot{E}$ and $\dot{L}$.

4.2 Climb to altitude with stall protection

The previous test case demonstrates the correct implementation of the TECS core coupled to the adopted variable-mass 3-DoF aircraft model. However, such longitudinal flight control system would be unable to safely operate the aircraft under a general sequence of requested variations of airspeed or altitude. In fact, the outer controller modelled by Eqs. (22) issues commands directly proportional to the airspeed and altitude signals' error. Nothing would prevent this module to provide excessively large inputs to the TECS core, which in turn would provide unrealistically large commands in thrust T_{c} and elevation angle θ_{c}. The aircraft may never be able to accurately track the intended airspeed and altitude. Even worse, it would quickly move out of its flight envelope, stalling or overspeeding to the ground. This is a natural limitation of the TECS core, which is agnostic of the aircraft flight dynamics and powerplant. Hence, it is imperative to include protections of the flight envelope, such that (i) the commanded flight path angle is within the allowable values - estimated with the Flight Mechanics equilibrium equations on a point-mass model - and (ii) the aircraft is made to accelerate if the airspeed is too close to the stall speed or decelerate if overspeeding. Thus, the flight-envelope protection is implemented upstream of the TECS core scheme and is based on the knowledge of the equilibrium boundaries of the open-loop system.

The protection system proposed in this research is first demonstrated here with a demanding climb simulation. The aircraft is initially trimmed at $V_0 = 82$ m/s and $h_0 = 1000$ m. The single setpoint on the altitude at the end of the climb is 6000 m while the setpoint on airspeed is kept to V_0. The initial airspeed is suitable to fly at low altitude, but it comes slightly below the stall speed for level flight at the target altitude. The flight envelope protection system, inserted before

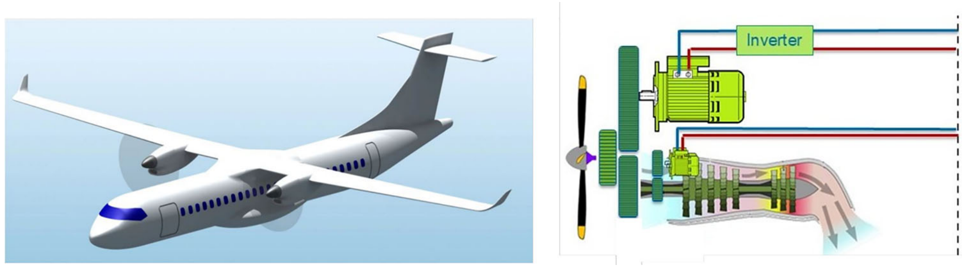

Fig. 4 Conceptual drawing of the Ultra Efficient Regional Aircraft (UERA)

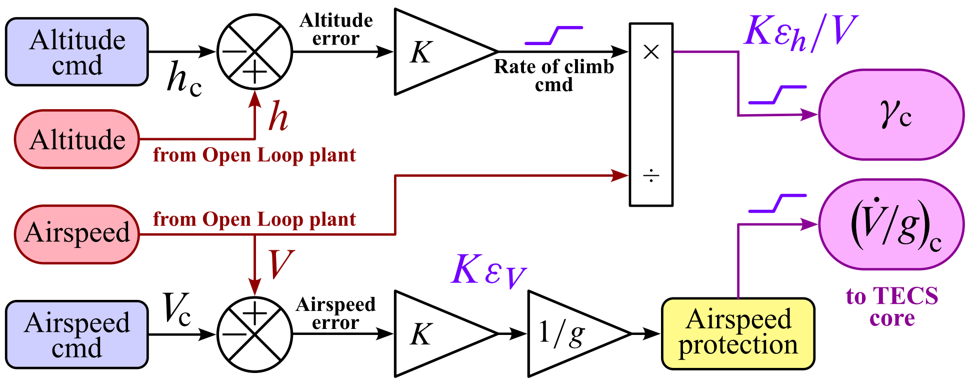

Fig. 5 Normalized commands generator block diagram

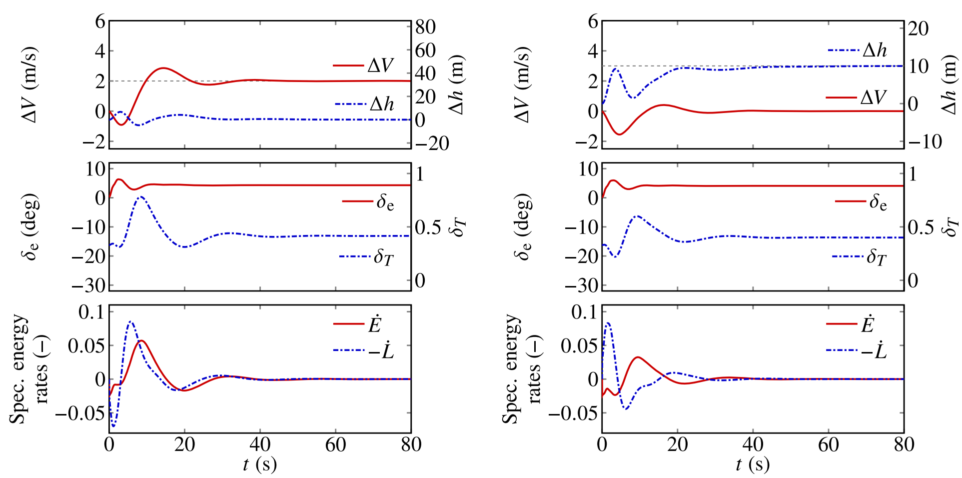

(a) Speed step demand $\Delta V_c = 2\,\text{m/s}$ with constant setpoint on altitude, $\Delta h_c = 0\,\text{m}$.

(b) Altitude step demand $\Delta h_c = 10\,\text{m}$ with constant setpoint on speed, $\Delta V_c = 0\,\text{m/s}$.

Fig. 6 Examples of TECS response decoupling. Starting from a trimmed level flight state, when only a setpoint step is commanded on speed or on altitude, respectively, the steady state responses are practically decoupled

the output $(\dot{V}/g)_c$ in Fig. 5, overrides the commanded airspeed signal and accelerates the aircraft to a higher velocity to keep a safety margin over the minimum speed. The implementation of such behavior is usually made with switches [21] and conditional if-else statements to opportunely process the desired signals. However, the integration of the flight dynamics module into the ODE4HERA Open Digital Platform requires its conversion into a Functional Mockup Unit (FMU) version 2.0. Such version cannot handle events such if-else logic, as they introduce discontinuities [23]. Therefore, all the necessary conditional statements throughout the Simulink implementation were programmed as smooth and differentiable functions. For instance, any switch that can be activated with a step command has been replaced with a hyperbolic tangent, whereas the if-else statements were replaced by algebraic operations.

In the case of the stall speed and overspeed protection, the flight control system overrides the target airspeed value, if the actual airspeed is too close to the flight envelope limits. The nominal commanded acceleration $(\dot{V}/g)_c$ is replaced by a smooth $(\dot{V}/g)_{\text{blend}}$ defined as:

$$\left(\frac{\dot{V}}{g}\right)_{\text{c,blend}} = \left(\frac{\dot{V}}{g}\right)_{\text{c}} + \sigma_{V,\min}\left(\frac{\dot{V}}{g}\right)_{\text{SR}} - \sigma_{V,\max}\left(\frac{\dot{V}}{g}\right)_{\text{OR}} \tag{23}$$

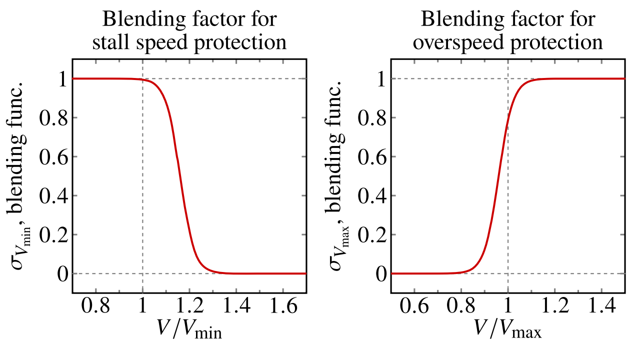

Fig. 7 Sigmoid functions defined in Eqs. (24)–(25) and used in Eq. (23) to enable airspeed protection from stall or overspeed. The differentiable form of the functions ensures compatibility with the FMI format. Value of the parameters: $k_V = 1.3$, $\tilde{V}_{\mathrm{min,offset}} = 2$, $\tilde{V}_{\mathrm{max,offset}} = 0.5$, $\Delta\tilde{V}_{\min} = \Delta\tilde{V}_{\max} = 0.08$

The blending functions $\sigma_{V,\{\min|\max\}}$ triggering the airspeed protection are:

$$\sigma_{V,\min} = \frac{1}{2}\left\{1 + \tanh\left[k_V\left(\tilde{V}_{\mathrm{min,offset}} + \frac{1 - V/V_{\min}}{\Delta\tilde{V}_{\min}}\right)\right]\right\} \tag{24}$$

$$\sigma_{V,\max} = \frac{1}{2}\left\{1 + \tanh\left[k_V\left(\tilde{V}_{\mathrm{max,offset}} + \frac{V/V_{\max} - 1}{\Delta\tilde{V}_{\max}}\right)\right]\right\} \tag{25}$$

where k_V is the slope of the curve, $\tilde{V}_{\mathrm{min,offset}}$ and $\tilde{V}_{\mathrm{max,offset}}$ are constant values anticipating the trigger at stall and overspeed onset, respectively, $V/V_{\min}$ and $V/V_{\max}$ are the ratios of current speed to minimum and maximum airspeed, respectively, $\Delta\tilde{V}_{\min}$ and $\Delta\tilde{V}_{\max}$ are parameters shaping the curves. Although the speeds $V_{\min}$ and $V_{\max}$ are functions of the altitude h, the ratios $V/V_{\min}$ and $V/V_{\max}$ eliminate this dependency, as shown in Fig. 7. The minimum speed protection is softly enabled from a 30% margin from the stall condition and fully engaged below the 10% margin. Conversely, the maximum speed protection is enabled starting at 20% margin from the overspeed condition and fully engaged when such condition has been achieved. The stall and overspeed recovery values $(\dot{V}/g)_{\{\mathrm{SR|OR}\}}$ in Eq. (23) are arbitrarily assigned as $(\dot{V}/g) = 0.1$.

Results of the simulation are shown in Fig. 8, where time histories of several variables are shown. The aircraft climbs from 1000 m to 6000 m as requested. However, the aircraft accelerates from the setpoint speed of $V_0 = 82$ m/s to keep a large margin from the theoretical level-flight stall speed. The commanded thrust is closely tracked throughout the simulation. Since it never saturates, no further protections of the flight envelope are needed, except the saturation on the commanded values of the pitch angle θ_c and the flight path angle γ_c. The former is arbitrarily limited within $-5°$ to $15°$ for passengers' comfort, whereas the maximum γ_c is limited to the theoretical limit $\gamma_{\max}$ in climb (occurring at stall speed), decreasing with altitude, and its minimum is limited to $-5°$ for passengers' comfort.

Notice how at the end of the climb (about 500 s) the airspeed drops to a value close to the stall speed, then increases later at about 700 s. This is due to the TECS energy management in this demanding condition. In fact, once the altitude is close to the target value, thrust is reduced to stop climbing. Since the aircraft has acquired both potential and kinetic energy after the injection of total energy due to thrust with the increasing airspeed, the elevator δ_e moves right after the throttle δ_T to split the energy rate, as TECS is struggling to recover the altitude overshoot while keeping a safety margin from stall speed. The elevation angle θ is kept large, while the commanded flight path angle γ_c is slightly negative until the target altitude is finally achieved and airspeed is increased to regain the safety margin from stall speed. A dangerously high attitude would have been reached, if the speed margin was tighter, as the flight control system would have decelerated the aircraft after the altitude overshoot due to the accelerated climb.

Being the aircraft a variable-mass system, the total fuel consumption is calculated by adding of the time integrals of the kerosene and hydrogen mass flow rates:

$$C_{\mathrm{ker}}(t) = \int_0^t \dot{m}_{\mathrm{ker}}\,\mathrm{d}\tau, \quad C_{H_2}(t) = \int_0^t \dot{m}_{H_2}\,\mathrm{d}\tau \tag{26}$$

These fuel masses are subtracted from the total aircraft mass during the mission, as shown in Fig. 8b.

4.3 Climb with maximum rate of climb tracking

This is an example of optimal performance tracking. Again, a climb from 1000 m to 6000 m is requested here. The target airspeed is a varying setpoint given by the aircraft maximum theoretical attainable climb rate, for the instantaneous vehicle mass and at the varying flight altitude. An a priori knowledge of the point-mass aircraft climb performance is required, so that the airspeed command is continuously updated into the Normalized Commands Generator of Fig. 5 as the altitude changes. Results are shown in Fig. 9. The initial airspeed $V_0 = 90$ m/s is sufficiently higher than the stall speed, therefore the commanded airspeed is accurately tracked as the flight control system aims at the optimal maximum climb rate, shown at the bottom of Fig. 9a. Throttle is mostly saturated at its maximum, as the commanded thrust matches the theoretical maximum value from the engine's deck.

The saturation of the commanded thrust signal T_c (Figs. 9 and 10) requires a special treatment of the TECS energy management. Since the total energy rate $\dot{E}$ is limited by the maximum thrust available, the flight control system may not satisfy both airspeed and altitude demands simulta-

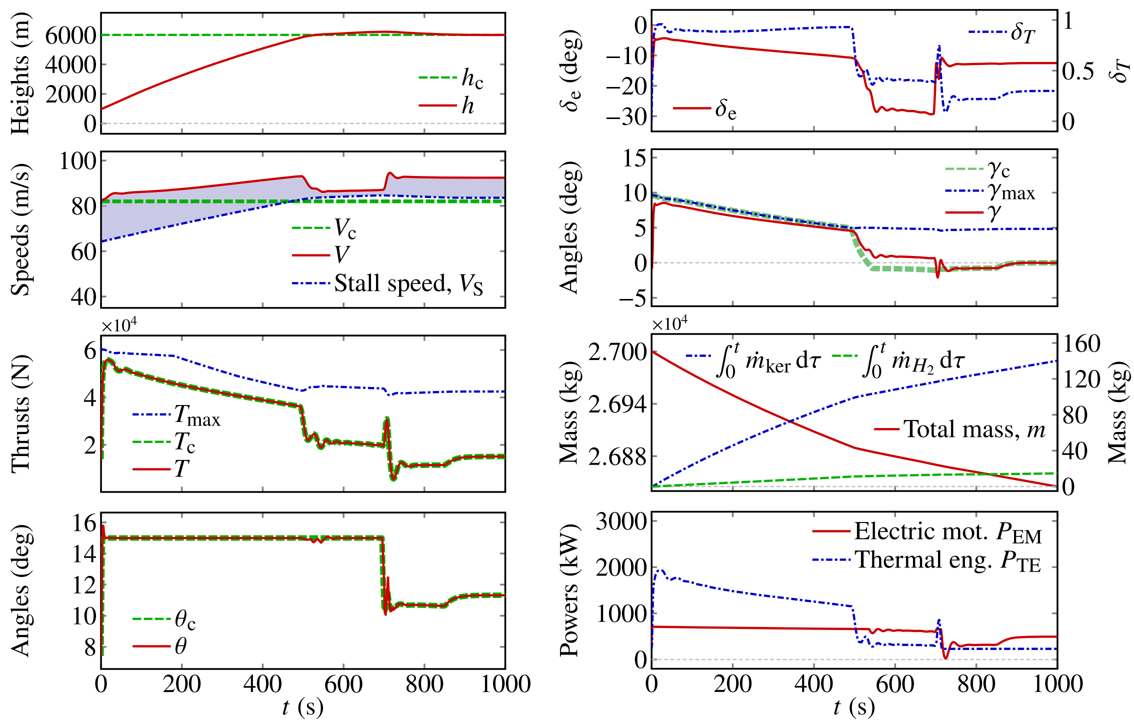

(a) A commanded altitude variation $\Delta h_c = 5000$ m, with a fixed commanded airspeed $V_c = 82$ m/s along the climbing path. A safe speed margin above the minimum speed is maintained, overriding the commanded value that would stall the aircraft at altitude. Thrust never saturates, while the pitch attitude is limited at 15°.

(b) Commanded inputs δ_T and δ_e. Commanded flight path angle γ_c equal the maximum attainable γ_{max} in the climb phase; the actual flight path angle γ does not fully track γ_c in climb due to envelope protection. Varying aircraft mass; consumed fuel masses, kerosene and hydrogen. Shaft power at each single thermal engine and electric motor.

Fig. 8 Example of demanding climb to altitude, with a low value of commanded speed, and TECS subjected to a stall speed protection algorithm

neously. At this point, a Control Authority Allocation (CAA) is introduced [4] to relax the commanded non-dimensional acceleration $(\dot{V}/g)_c$ or the commanded flight path angle γ_c when thrust saturates. Speed has control priority on flight path when the thrust command is at its upper or lower limit and $\gamma_c > 0.5\,\dot{E}$. If thrust saturates but $\gamma_c \leq 0.5\,\dot{E}$, flight path angle is given priority on elevator control. With this logic, for relatively large γ_c at full thrust (e.g. demanding climb), the flight path angle is allowed to wander while airspeed is tracked accurately. Conversely, in shallow accelerating climbs or soaring descents and dives the commanded flight path is accurately followed, while the airspeed command may not be met. When thrust is not saturated, TECS operates in its nominal regime, since there is sufficient power to track both altitude and airspeed simultaneously.

The triggering of the Speed-on-Elevator Control Priority (SoECP) is shown in Fig. 10. As the commanded thrust T_c saturates to the maximum thrust T_{max} and the commanded flight path angle γ_c is bigger than the half of the specific energy rate $\dot{E}$, SoECP is smoothly enabled by the combination of two activation functions modeled as hyperbolic tangent. Elevator moves to accurately track the commanded airspeed, while the flight-path angle may drift from the intended value (Fig. 9b). In this particular application, such flight path deviation is not appreciable, since the accurate tracking of the airspeed at the maximum rate of climb corresponds to the intended flight path angle. The opposite maneuver, requesting a descent at constant speed and prompting again for elevator control priority, is shown in the next section.

4.4 Descent with path-on-elevator control priority

In this example, the aircraft is required to descend from 6000 m to 1000 m, while keeping the initial airspeed $V_0 = 100$ m/s. Results are shown in Fig. 11. As the aircraft descends, it converts its potential energy into kinetic energy. However, the assigned conditions are such that kinetic energy is in excess with respect to the required total energy to fly at the same airspeed at a much lower altitude. Thrust saturates to idle, while the commanded potential energy rate $\gamma_c < 0$. Since the aerodynamic drag is insufficient in reducing the total energy in descent, the CAA is invoked to give prior-

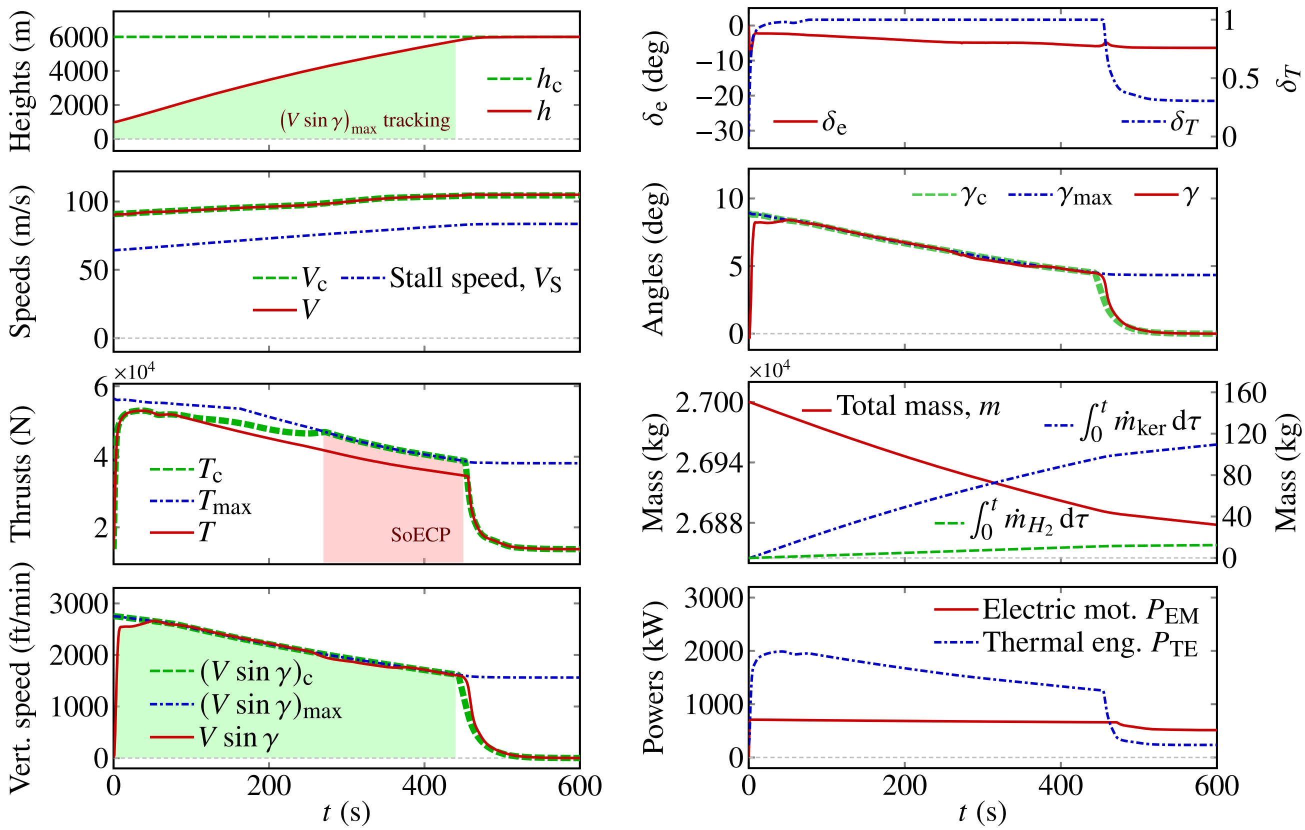

(a) A commanded altitude variation, with a varying commanded airspeed that tracks the maximum rate of climb performance. Thrust profile saturating at high altitude, prompting for elevator control priority.

(b) Elevator is pulled despite the increasing airspeed to keep the the commanded flight path angle as the aircraft climbs at full throttle. Varying fuel and aircraft masses. Electric motor at full power, boosting the thermal engine.

Fig. 9 Example of variable setpoint tracking. The climb to altitude is accomplished by tracking the state of maximum attainable rate of climb $(V \sin\gamma)_{max}$, which varies with altitude and speed

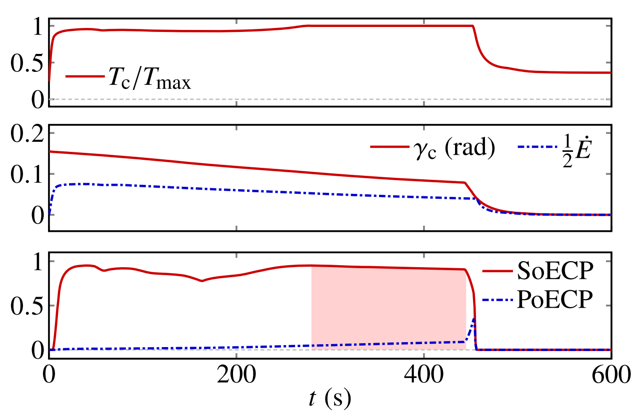

Fig. 10 Time histories demonstrating the Control Authority Allocation (CAA) for the simulation of Fig. 9. Speed-on-Elevator Control Priority (SoECP) is smoothly engaged as the commanded thrust saturates to maximum and the required potential energy rate γ_c is larger than half of the total energy rate $\dot{E}$

ity to flight path tracking. Path-on-Elevator Control Priority (PoECP) is enabled and airspeed is let wander. In fact, the airspeed increases as the aircraft descends, while thrust is in idle and the flight path is followed within the limits of the flight envelope. The elevation angle θ is reduced, while the aircraft accelerates and the flight path angle γ is approximately held constant. The consumption of the fossil fuel is non-zero, despite the idling thrust. In fact, the gas turbine power has a minimum value in idling conditions, as the thermal engine cannot be turned off for both safety and on-board systems' powering. Conversely, the electric motor is turned off when $T = 0$ and consequently the hydrogen's consumption is null.

The enabling of the PoECP function is shown in Fig. 12. The saturation of the commanded thrust T_c to zero and the $\gamma_c < 0.5\,\dot{E}$ activates the path control priority quickly, but smoothly. However, CAA alone is not sufficient to safely bring the aircraft to the required low altitude. The aircraft may overshoot the target altitude, if the rate of descent is

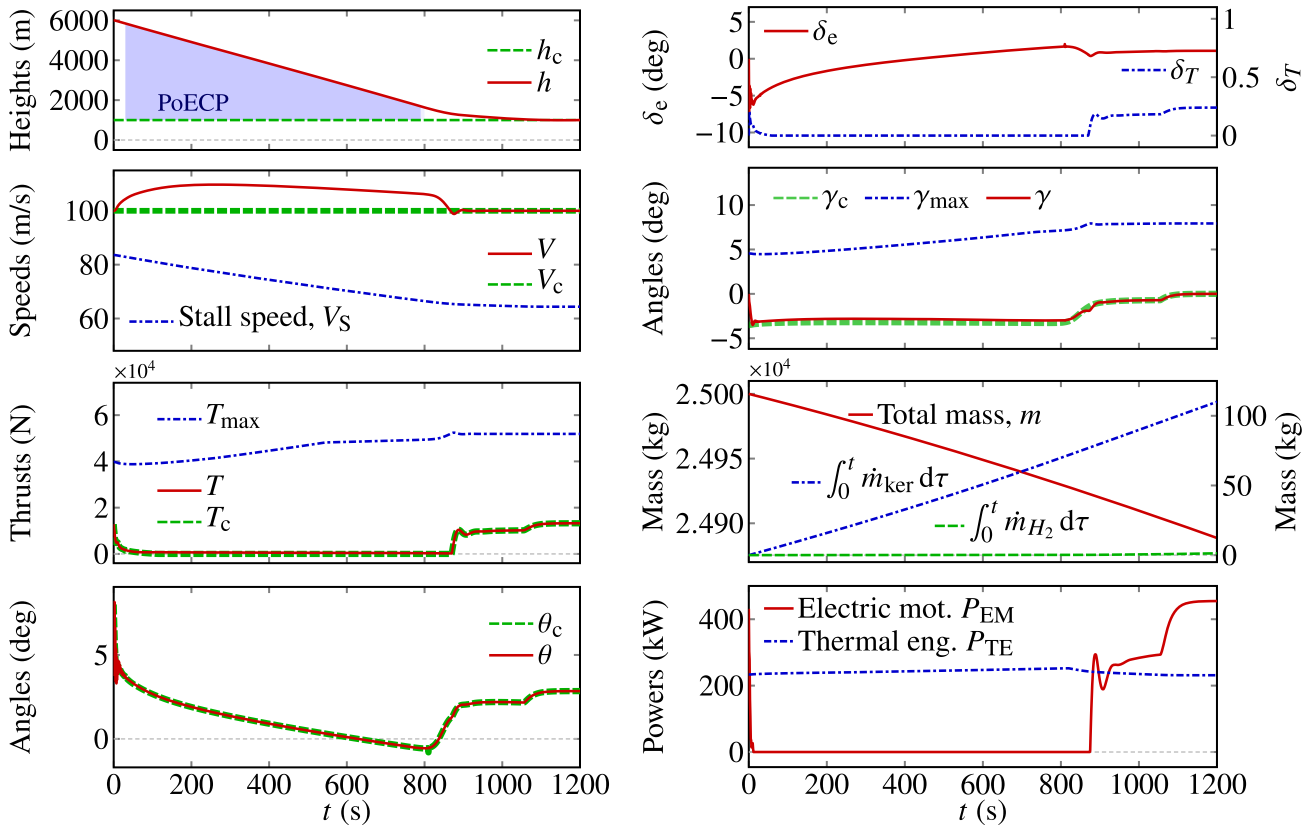

(a) The assigned descent profile requires idling engines. Thrust saturates to zero, altitude is accurately tracked, while airspeed is let wander within the flight envelope limits. The actual thrust and pitch attitude smoothly track the commanded profiles, which are generated by the TECS Core algorithm.

(b) Commanded inputs δ_T and δ_e. Commanded flight path angle γ_c, negative during the descent phase then zero during the level flight phase. Varying aircraft mass; consumed fuel masses, kerosene and hydrogen. Minimum power kept by the thermal engine, while the electric motor is turned off.

Fig. 11 Example of demanding descent, with a commanded altitude variation $\Delta h_c = -5000$ m and a fixed commanded airspeed $V_c = 100$ m/s along the descending path. The descent is followed by a level flight phase at the final altitude

not properly saturated. This is dangerous when descending to an altitude close to the ground. A constant limit for the rate of descent set by passenger's comfort is not sufficient, as a low value would make the descend maneuver unreasonably long. Therefore, a dynamic saturation for the maximum rate of descent (not shown in the simplified scheme of Fig. 5) has been added in the Normalized Commands Generator after the upper gain K. The maximum negative $\dot{h}$ is reduced as the altitude error ε_h is close to zero. This explains the slope change in altitude tracking at the top of Fig. 11a.

4.5 Reference mission profile

This final application shows the aircraft behavior managed by the flight control system with a typical mission profile. The sequence of altitude and airspeed setpoints is presented in Table 2. The mission starts with the airborne aircraft from the end of take-off path. The aircraft performs a two-segment climb with a speed step, then accelerates at cruise altitude. After the cruise phase, it performs a two-segment descent reducing the airspeed at each step. Simulation ends at the final altitude, which is equal to the initial altitude, with a level flight.

Results are shown in Figs. 13 and 14. It can be observed how the aircraft follows the assigned mission profile. In the first climb segment the aircraft flies at constant speed, while it accelerates to the en-route speed in the second climb segment (Fig. 13a). These conditions require full throttle, especially at the beginning of each phase (Fig. 13b), prompting for CAA engaging speed control priority in climb and path control priority at the beginning of the cruise and for most of the descent phases (Fig. 14). In particular, the second descent phase requires a significant deceleration. Therefore, the PoECP function lets airspeed wander while TECS aims

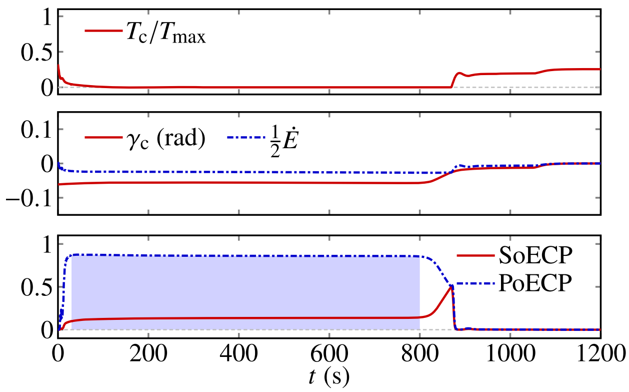

Fig. 12 Time histories demonstrating the Control Authority Allocation (CAA) for the simulation of Fig. 11. During the descent phase, the commanded thrust T_c saturates to zero and $\gamma_c < \frac{1}{2}\dot{E}$. The CAA gives priority to path tracking, enabling the Path-on-Elevator Control Priority (PoECP), letting airspeed move from the commanded value. When the commanded altitude is reached, the nominal TECS algorithm is restored and the CAA is disabled

Table 2 Mission profile

Phase	Start alt. (m)	End alt. (m)	Airspeed (m/s)
Initial climb	500	(A) 1500	(A) 100
En-route climb	1500	(B) 6000	(B) 110
Cruise	6000	(C) 6000	(C) 140
Descent high	6000	3000	120
Descent low	3000	500	90

Sequence of altitude and airspeed setpoints A–B–C shown in the flight envelope plot of Fig. 16

at flight path tracking. The elevation and flight path angles are accurately followed within their limits throughout the mission. The time histories of the gas turbine and electric motor powers allow an accurate evaluation of the kerosene and hydrogen consumptions.

The profiles of altitude and hybridization factor vs. range are shown in Fig. 15. The airplane covers about 400 km in an hour. All the main mission phases are accurately simulated, except for take-off and landing, which are out of the scope of this work. The hybridization factor Φ shows the significant contribution of the electric motor to the mission execution. The ratio of electric power to the total mechanical power is between 60% and 70% when thrust does not saturates. The electric motor is acting as a booster for the powerplant when maximum thrust is required, while it is turned off when the aircraft is descending with idle throttle.

5 Insights and discussion

The simulations presented in Sect. 4 have shown the capabilities of TECS applied to the hybrid-electric airplane model under study in various operational scenarios. Integrating modules such as the CAA, stall-speed, and terrain-protection systems into the core simulation framework enables to achieve challenging combinations of target airspeed and altitude values.

The aircraft level-flight envelope is shown in Fig. 16, illustrating the allowable combinations of airspeed and altitude in constant-altitude and steady flight. The limits are represented by the stall speeds on the left, the maximum speeds on the right, and the service ceiling on top (defined as the altitude where a maximum residual vertical speed of 200 ft/min occurs). Contours of theoretical maximum rate of climb are also shown. In the same figure, two trajectories in the plane (V, h) are traced from two selected simulation results: the fastest climb from 1000 m to 6000 m, presented in Sect. 4.3, and the first three phases (two-segment climb and cruise) of the typical mission profile, introduced in Sect. 4.5. In the first case (S-E), the tracking of the maximum rate of climb is apparent. The aircraft adapts its velocity during climb to match the maximum vertical airspeed represented by the contour plot. The second trajectory (S-A-B-C) exhibits a first climb segment (S-A) flown at almost constant speed. A second segment (A-B) follows, where the aircraft accelerates while climbing, achieving first the target airspeed and then proceeding at constant airspeed until cruise altitude is reached. The last segment (B-C) represents the acceleration to cruise airspeed at the final constant altitude setpoint.

The complex interactions among the aircraft dynamics, the hybrid-electric power plant model, and the energy management of the flight control system are accurately captured by the developed simulation tool. A high-level objective of such a tool is to provide accurate time histories of propulsive power utilization and fuels consumption. For instance, in the full mission simulation presented in Sect. 4.5, the plots in Fig. 13b show that a high value of the hybridization factor can potentially save fossil fuel burn and reduce pollutants emission. Having established and simulated a reference aircraft model with its advanced flight control system, this prompts for future parametric investigations of the power plant hybridization.

To complement the scenario-based examples and assess the robustness of the continuous stall-protection logic - that is, the most critical among all the envelope protections implemented in this study -, a Monte Carlo campaign was performed over randomized initial conditions and altitude/speed commands within the flight envelope. The proposed TECS with the envelope-protection controller and the hybrid-propulsion model were not retuned. In all simulations, the aircraft was initially trimmed at an airspeed-to-stall-speed ratio $(V/V_S)_0 = 1.3$, and simultaneous altitude and airspeed steps were commanded, from h_0 to h_{final} and from V_0 to V_{final}, respectively. The ranges of commanded values were established as follows: $0\,\text{m} \leq h_0 \leq h_{\text{final}} \leq 8000\,\text{m}$

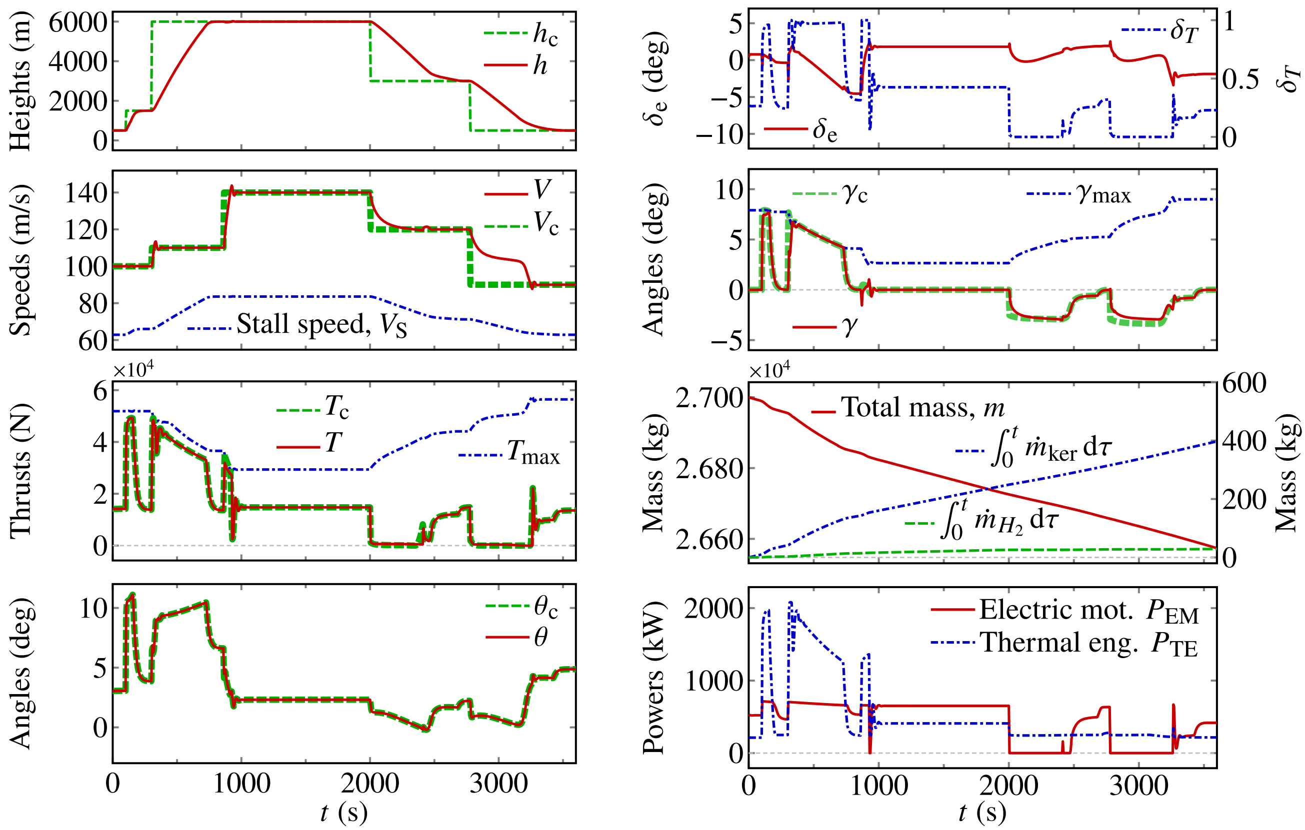

(a) A standard two-segment climb to cruise altitude then a constant-altitude acceleration to cruise speed. The remaining segments reproduce a cruise phase followed by a descent to the final altitude. TECS accurately tracks both altitude airspeed when thrust does not saturates. The pitch attitude θ profile also tracks the commanded value as demanded by TECS.

(b) Inputs provided by TECS to the open-loop plant model, δ_T and δ_e. Commanded γ_c and actual γ flight path angles, compared to the maximum achievable values in climb. Varying aircraft mass and consumed fuel masses, kerosene and hydrogen. Shaft power at each single thermal engine and electric motor.

Fig. 13 Example of typical mission profile used as a reference for assessing the hybrid-electric aircraft performance. The mission includes a two-segment climb, a cruise phase, and a two-segment descent. The simulation scenario starts at the assumed end of the standard take-off path, and terminates right before the approach and landing phase

and $1.0 \leq (V/V_S)_{final} \leq 1.2$. These settings ensured the activation of stall protection in all simulation samples while remaining inside the flight envelope. For each run, the minimum ratio $(V/V_S)_{min}$, the final ratio $(V/V_S)_{final}$, and the normalized maximum altitude h_{max}/h_{final} were observed.

The total number of Monte Carlo runs was selected based on a pilot campaign of 500 simulations. The resulting variance estimates for $(V/V_S)_{final}$ and $(V/V_S)_{min}$ were used in standard sample-size calculation formulas to achieve an absolute error of $\pm 0.2\%$ on the mean with 95% confidence, and to reliably capture the first percentile with a $\pm 0.5\%$ error. These calculations suggested a minimum required Monte Carlo sample size of 2900 runs, to ensure statistically robust estimates of both average and minimum speed margin over V_S.

The probability density functions of $(V/V_S)_{final}$ and $(V/V_S)_{min}$ are shown in Fig. 17, where a larger variance of the minimum speed ratio is apparent. The stochastic convergence of $(V/V_S)_{min}$ is shown in Fig. 18. Its progressive mean μ is trending toward 1.118, and remains consistently within the desired error band of $\pm 0.2\%$. The first percentile P_1 of $(V/V_S)_{min}$ becomes stable at 1.03 after a few hundred runs. The simulation campaign statistics are reported in Table 3. The value $P_1 = 1.03$ indicates that in the 99% of simulated maneuvers the minimum speed during the transient is at least 3% higher than the stall speed. In the remaining 1% of all sampled simulations, the minimum observed speed

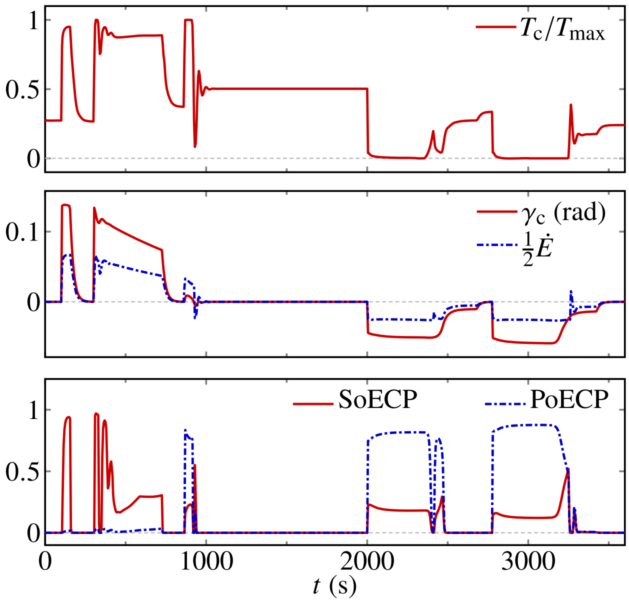

Fig. 14 Time histories demonstrating the Control Authority Allocation (CAA) for the simulation of Fig. 13. When commanded thrust saturates to the maximum available value during the climb phase, the SoECP function is smoothly engaged and the airspeed tracking assumes priority on the elevator. When the commanded altitude is reached, the nominal TECS algorithm is restored and the CAA is disabled. In the descent phase, the PoECP function is enabled when the commanded thrust T_c saturates to zero, such that flight path angle has priority on the elevator

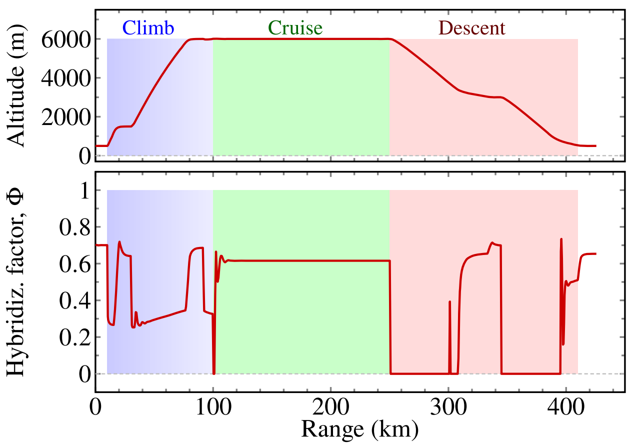

Fig. 15 Altitude vs. range profile (Top) for the mission simulation of Fig. 13. Hybridization factor Φ vs. range profile (Bottom) for the same mission. The nonzero profile of Φ shows how the electric motors are used during the whole mission, with a significant contribution during the phases where thrust does not saturate

falls within 1.01 and 1.03 V_S. The average value of the minimum speed during the transient is about 12% higher than stall speed. Steady state values (V_{final}) have sensibly larger values, with an average airspeed 16% higher than stall speed and a minimum value of 1.11 V_S. This means that the implemented envelope protection strategy is effective in avoiding the stall condition.

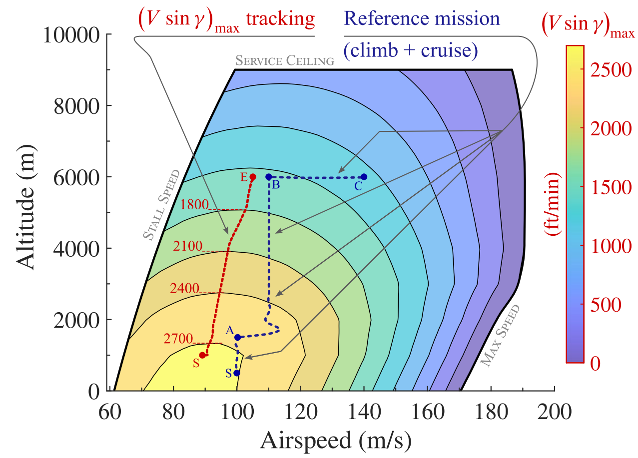

Fig. 16 Traces in the aircraft flight envelope plane (V, h) of the simulation examples presented in Sects. 4.4 and 4.5. (Left trace) Maximum climb rate tracking, from start S to end E. See Fig. 9a. (Right trace) Only the climb and cruise phases are shown for clarity, from start S to setpoints A–B–C. See Fig. 13a and Table 2

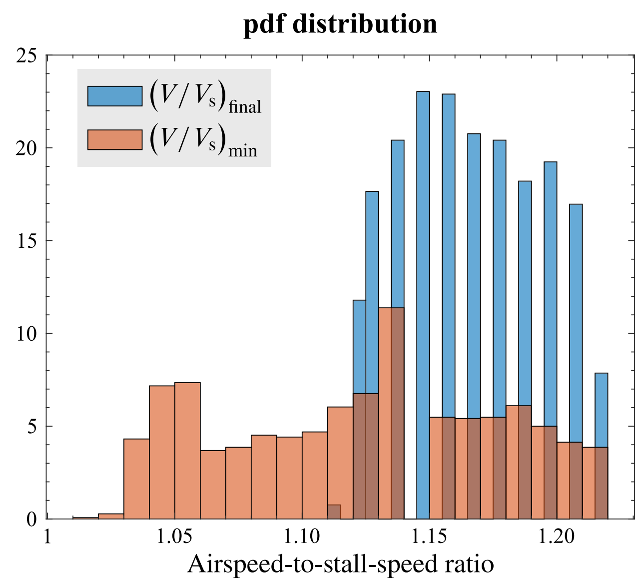

Fig. 17 Stall-speed protection Monte Carlo simulations; sample size of 2900. Probability density function of ratio's V/V_S minimum and final values once the step response has risen, reached when the envelope protection is triggered

Table 3 Statistics of the observed variables in the Monte Carlo campaign

	Mean	Std. dev	First perc	Min
$(V/V_S)_{min}$	1.118	0.0549	1.03	1.01
$(V/V_S)_{final}$	1.168	0.0285	1.12	1.11

Sample size of 2900 simulations

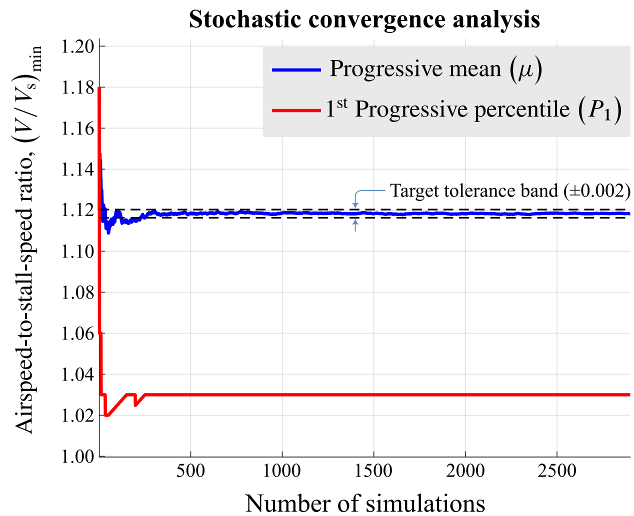

Fig. 18 Monte Carlo simulations assessing the robustness of stall speed protection algorithm. Variation of the mean value of $(V/V_S)_{min}$ reached in 2900 simulation scenarios where the envelope protection is triggered

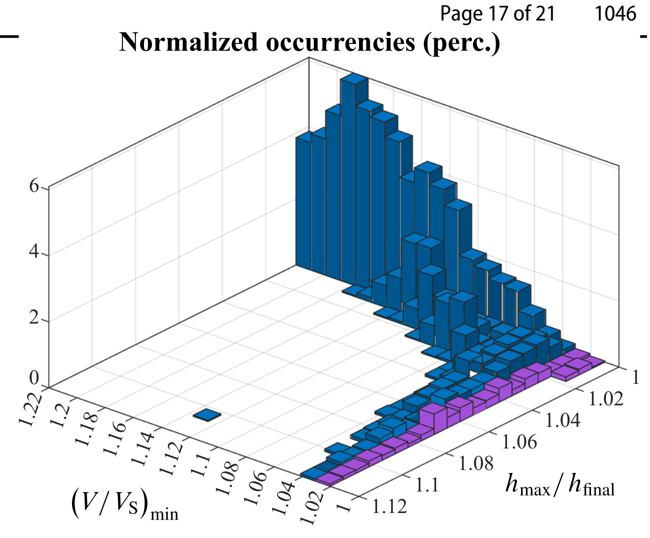

Fig. 19 Stall-speed protection Monte Carlo simulations. Normalized occurrencies (percentage) distribution versus $(V/V_S)_{min}$ and h_{max}/h_{final}. First percentile P_1 of $(V/V_S)_{min}$ colored differently

Finally, a relationship between $(V/V_S)_{min}$ and h_{max}/h_{final} can be observed. As presented in the example of Fig. 8a, $(V/V_S)_{min}$ may become very close to 1 when an altitude overshoot occurs. This causes the flight control system to derate thrust and make the aircraft descend; the side effect is an airspeed reduction. Therefore, it is expected that: $(V/V_S)_{min}$ is closer to 1 when the ratio h_{max}/h_{final} is large - that is, altitude overshoot is large -, and $(V/V_S)_{min} \approx (V/V_S)_{final}$ when the altitude overshoot is small. This is confirmed by the bi-variate histogram in Fig. 19 showing the combined occurrences of airspeed and altitude ratios. The observed values of $(V/V_S)_{min}$ are distributed at the boundaries of the numerical domain. For $h_{max}/h_{final} \approx 1$, the histogram bins are relatively tall for $(V/V_S)_{min} > 1.10$ while many short bins are found for $h_{max}/h_{final} > 1.02$ and $(V/V_S)_{min} < 1.06$, indicating that altitude overshoot is critical for the above mentioned thrust reduction, further reducing the stall speed margin during the step commands transient.

Across the randomized climb/deceleration scenarios considered, the continuous stall-protection function consistently maintained airspeed above stall, confirming a robust behavior of the envelope-protection system over a wide range of operating conditions.

6 Conclusion

This research demonstrates a successful application of TECS to a fully nonlinear model of hybrid-electric fixed-wing aircraft. The presented mission control examples feature the time histories of the hybridization factor and fuels consumption, providing an accurate evaluation of the commercial performance and environmental impact of the hybrid-propulsion architecture.

The outcome of several simulated maneuvers show that the TECS core algorithm is able to manage the energy states of the aircraft, ensuring coordinated control of thrust and elevator to achieve decoupled command responses. This unification of longitudinal controls through total energy principles enables a human-like behavior, overcoming the limitations of the separate autopilot and autothrottle implementations.

A set of 2900 Monte Carlo simulations has shown that the proposed flight-envelope protection strategy is robust and can be used for a wide range of flight conditions requiring a low-speed climb.

The simulation framework is also able to track an optimum performance like the fastest climb. In this case, the target airspeed is continuosly updated to maximize the vertical speed of the aircraft. Under demanding flight conditions, where the commanded thrust saturates, a Control Authority Allocation logic and an anti-windup algorithm for the integrator ensure proper energy management. Although TECS is known to work on different aircraft classes, the implementation on a specific aircraft still requires a careful and manual preprocessing of the flight envelope boundaries: stall, overspeed, climb performance, service ceiling, and power plant characteristics. Further, the heuristic tuning of TECS gains, although not requiring scheduling with airspeed and altitude, is a known limitation.

The framework developed in Simulink is decomposable in different submodules and exportable as multiple FMUs for integration into third-party digital platforms. At this scope, the flight envelope protection system, as well as CAA and other dynamic saturations, were implemented with smooth activation functions, enabling compliancy to the openness

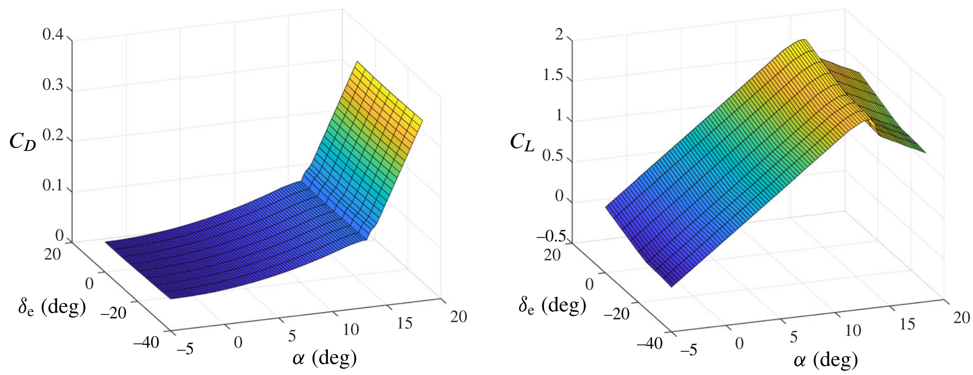

Fig. 20 Nonlinear dependency of drag coefficient C_D and lift coefficient C_L on angle of attack α and elevator deflection δ_e

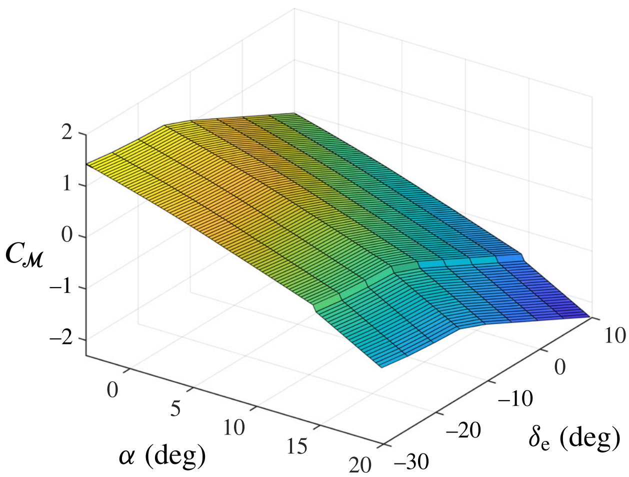

Fig. 21 Nonlinear dependency of pitching moment coefficient $C_{\mathcal{M}}$ on angle of attack α and elevator deflection δ_e

requirement of solution-neutral architectures (independency from specific software solutions).

This work can be expanded in different directions. For instance, the total energy principles can be applied to the lateral-directional dynamics. Alternatively, a propulsion energy management can be developed to optimize the hybridization factor at runtime. Any improvement to this research work will make possible to simulate even more realistic navigation scenarios.

Appendix A Aerodynamic model of the reference hybrid-electric aircraft

The hybrid-electric aircraft selected for this research incorporates the nonlinear aerodynamic model that is summarized here. Each aerodynamic coefficient is a function of state and input variables, which is expressed as a sum of nonlinear terms, commonly known as aerodynamic build-up formula. All angles in the expressions below are in degrees. The drag coefficient C_D is a nonlinear function of the angle of attack α and of the elevator deflection angle δ_e:

$$C_D = f(\alpha, \delta_e) \tag{A1}$$

where f is a tabular function represented in Fig. 20 (left). The lift coefficient C_L is a function of the angle of attack α, of the elevator deflection angle δ_e, and of unsteady and dynamic terms:

$$C_L = g(\alpha, \delta_e) + C_{L_{\dot{\alpha}}} \hat{\dot{\alpha}} + C_{L_q} \hat{q} \tag{A2}$$

where g is a tabular function represented in Fig. 20 (right), $\hat{\dot{\alpha}} = \dot{\alpha}\bar{c}/(2V)$ is the nondimensional angle of attack rate, $\hat{q} = q\bar{c}/(2V)$ is the nondimensional pitch rate, $C_{L_{\dot{\alpha}}} > 0$ is the unsteady lift derivative, and $C_{L_q} > 0$ is the dynamic lift derivative. Similarly, the pitching moment coefficient $C_{\mathcal{M}}$ is a function of the angle of attack α, of the elevator deflection angle δ_e, and of unsteady and dynamic terms:

$$C_{\mathcal{M}} = m(\alpha, \delta_e) + C_{\mathcal{M}_{\dot{\alpha}}} \hat{\dot{\alpha}} + C_{\mathcal{M}_q} \hat{q} \tag{A3}$$

where m is a tabular function represented in Fig. 21, $C_{\mathcal{M}_{\dot{\alpha}}} < 0$ is the unsteady pitch derivative, and $C_{\mathcal{M}_q} < 0$ is the pitch damping derivative.

The aerodynamic and propulsive models are properties of their respective owners in the HERA project, who shared these data among a restricted number of ODE4HERA partners under a Consortium Agreement. As such, the data used in this work are not exactly those produced within the HERA project, although they likely represent such kind of regional hybrid-electric aircraft.

Appendix B Propulsive model of the reference hybrid-electric aircraft

The contour maps of Fig. 22a, b show the dependency of thrust delivered by the single propeller on the true airspeed V at different shaft power values and two altitudes. Shaft power P_{sh}, which accounts for mechanical losses due to gearboxes,

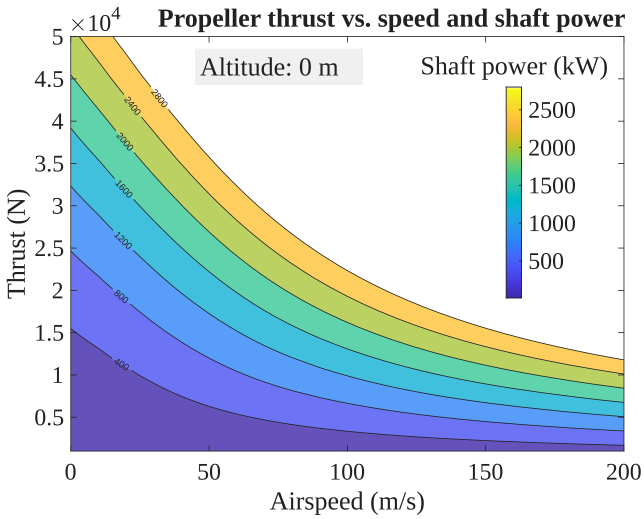

(a) Thrust delivered at Sea level altitude by the single propeller at given values of the airspeed and shaft power delivered by the coupled hybrid-electric system.

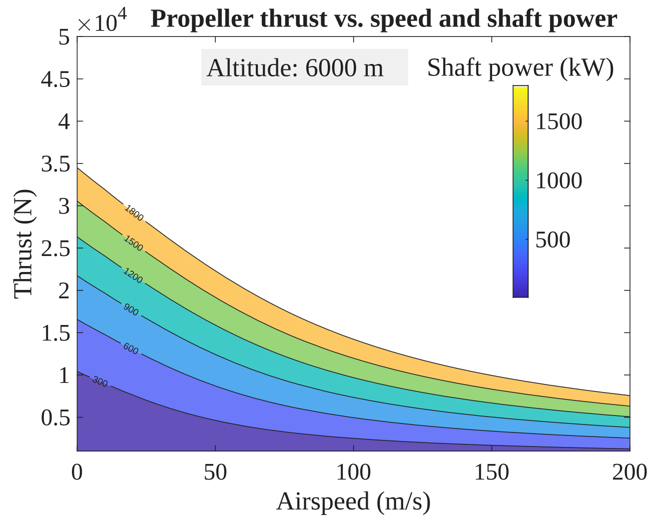

(b) Thrust delivered at $h = 6000$ m by the single propeller at given values of the airspeed and shaft power delivered by the coupled hybrid-electric system.

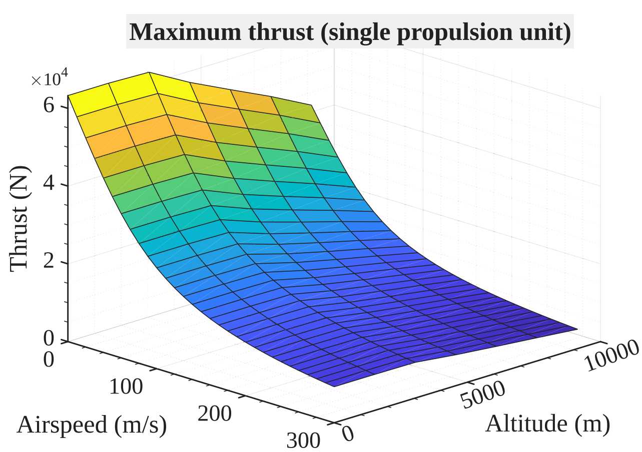

(c) Maximum available thrust per propulsive unit, as a function of altitude and airspeed.

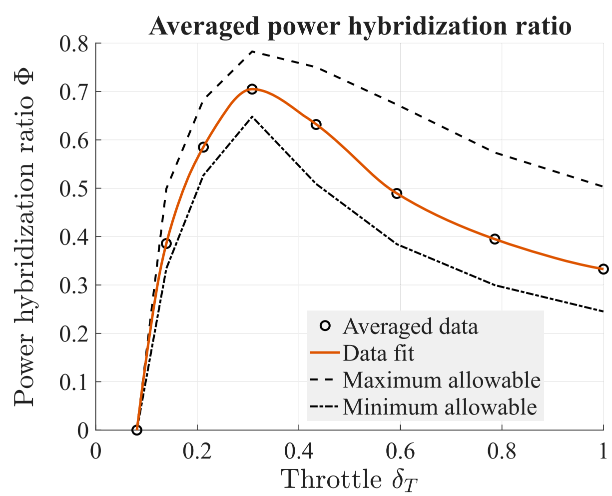

(d) Hybridization factor Φ, cfr. Equation (14), as a function of the throttle setting δ_{T}.

Fig. 22 Propulsion system data obtained from a reference engine deck, based on an integrated design of fuel cell, electric motor, thermal engine and propeller, for the hybrid-electric regional transport aircraft considered in this study

is a function of throttle setting δ_{T}, flight altitude h, and Mach number $M = V/a(h)$. The resulting thrust model is a nonlinear function of a point in the space (V, P_{sh}), that captures the complex interactions between the propulsion system and the operable flight conditions.

For each point (V, h) within the flight envelope, by setting the throttle $\delta_{\mathrm{T}} = 1$, the resulting thrust has a maximum value $T_{\max}(V, h)$, which is the maximum available thrust in that flight condition. Shown in Fig. 22c, this maximum thrust is a key parameter for the design of the control system, as it represents the upper limit of the control authority available to the pilot. The actual thrust is a tabulated function of $\delta_{\mathrm{T}} \in [0, 1]$, V, and h.

Figure 22d shows a simplified dependency of the hybridization factor Φ on δ_{T} where the effects of M and h have been averaged.

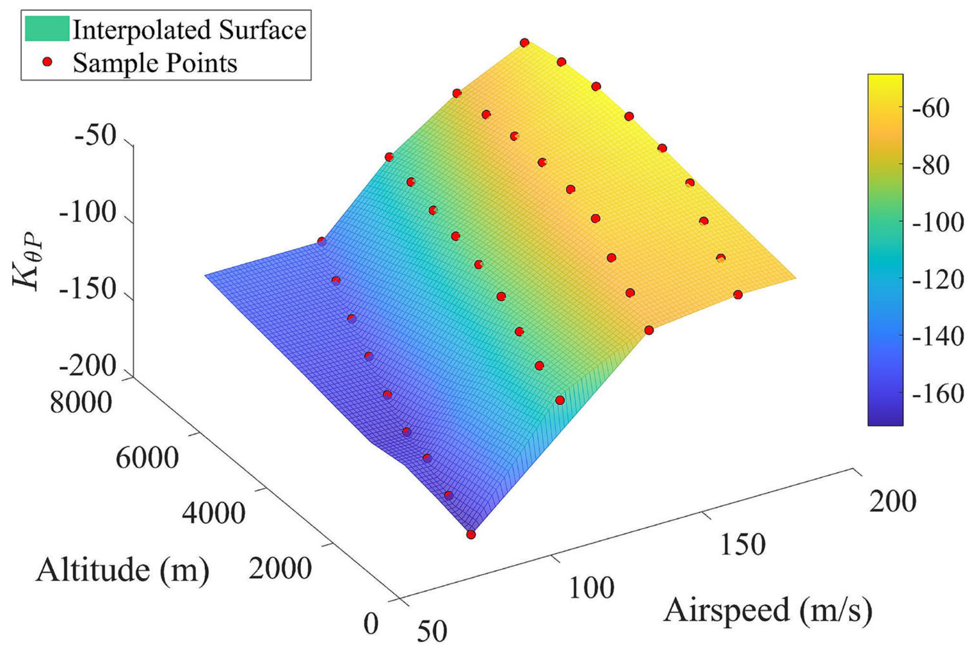

Fig. 23 Nonlinear dependency of scheduled proportional gain $K_{\theta \mathrm{P}}$ of the autopilot SISO system on altitude and airspeed

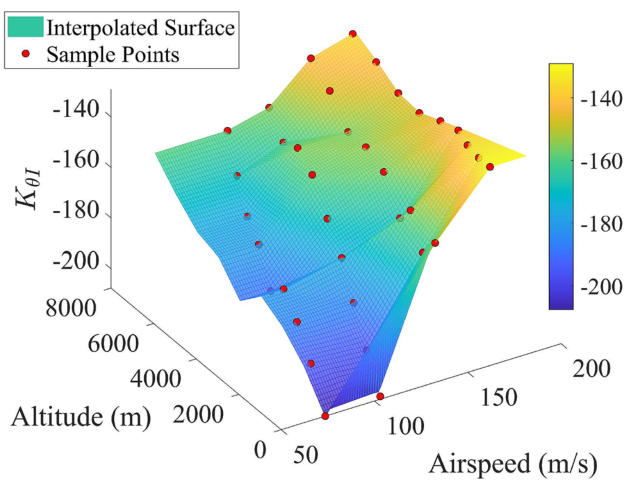

Fig. 24 Nonlinear dependency of scheduled integral gain $K_{\theta \mathrm{I}}$ of the autopilot SISO system on altitude and airspeed

Appendix C Inner-loops scheduled gains

Examples of scheduled gains of the inner-loop (aircraft-dependent) controllers are here reported. The gain scheduling is based on the altitude h and airspeed V of the aircraft, and is designed to ensure stability and performance across the flight envelope. As the aircraft moves in the (V, h) plane, controllers' gains are continuously updated. The response surfaces, like those shown in Figs. 23 and 24, were generated by interpolating many sample points, which in turn were obtained by locally tuning the inner-loop controllers. Tuning was performed in MATLAB by first linearizing the open-loop plant about each trim point, then defining the transfer function of each linearized plant, and finally setting the desired response for a step command of δ_{e} and δ_{T}.

Acknowledgements This work has been carried out within the European research project ODE4HERA (Project Number: 101140510), supported by the Clean Aviation Joint Undertaking and its members. Co-Funded by the European Union. Views and opinions expressed are however those of the author(s) only and do not necessarily reflect those of the European Union or Clean Aviation Joint Undertaking. Neither the European Union nor the granting authority can be held responsible for them.

Author contributions All authors contributed to the conception and design of the present study. D. C. and A.D.M. performed all the following tasks in synergy: model development, control-system implementation, simulation activities, post-processing of results. The first draft of the manuscript was written by A.D.M., and all authors commented on previous versions of the manuscript. All authors read and approved the final manuscript.

Funding Open access funding provided by Università degli Studi di Napoli Federico II within the CRUI-CARE Agreement. This study was supported by Clean Aviation Joint Undertaking and its members. Co-Funded by the European Union. Open access funding provided by Università degli Studi di Napoli Federico II within the CRUI-CARE Agreement.

Data availability Restrictions apply to the availability of these data. Except for those shown in the paper, data were obtained from HERA consortium and are not available for release.

Declarations

Conflict of interest The authors declare that they have no conflict of interest.

Consent for publication The authors grant the journal of Nonlinear Dynamics the authority to publish this work.

References

1. Graham, D., McRuer, D.T.: Analysis of Nonlinear Control Systems. Dover Publications, New York (1971)
2. Lambregts, A.A.: Vertical flight path and speed control autopilot design using total energy principles. AIAA Paper (83-2239) (1983). https://doi.org/10.2514/6.1983-2239
3. Amelink, M., Mulder, M., Van Paassen, M.M., Flach, J.: Theoretical foundations for a total energy-based perspective flight-path display. Int. J. Aviat. Psychol. **15**, 205–231 (2005). https://doi.org/10.1207/s15327108ijap1503_1
4. Lambregts, A.A.: TECS generalized airplane control system design—an update. In: Advances in Aerospace Guidance, Navigation and Control, pp. 503–534. Springer, Berlin, Heidelberg (2013). https://doi.org/10.1007/978-3-642-38253-6
5. Lambregts, A.A.: THCS generalized airplane control system design. In: Advances in Aerospace Guidance, Navigation and Control. Delft, The Netherlands. https://api.semanticscholar.org/CorpusID:202713230 (2013)
6. Bruce, K.R., Kelly, J.J., Person Jr, L.H.: NASA B737 flight test results of the Total Energy Control System. In: Astrodynamics Conference. American Institute of Aeronautics and Astronautics, Reston, VA (1986). https://doi.org/10.2514/6.1986-2143
7. Faleiro, L.F., Lambregts, A.A.: Analysis and tuning of a 'Total Energy Control System' control law using eigenstructure assignment. Aerosp. Sci. Technol. **3**(3), 127–140 (1999). https://doi.org/10.1016/S1270-9638(99)80037-6
8. Spark, H., González, P.J., Ruwisch, C., Meyer-Brugel, W., Silvestre, F.J.: An assessment of aircraft control via SISO control loops and total energy control. Technical Report 550216, Deutsche Gesellschaft für Luft- und Raumfahrt - Lilienthal-Oberth e.V. (2021). https://doi.org/10.25967/550216
9. Shevchenko, A.M.: Energy-based approach for flight control systems design. Autom. Remote. Control. **74**(3), 372–384 (2013). https://doi.org/10.1134/S0005117913030041
10. Jimenez, P., Lichota, P., Agudelo, D., Rogowski, K.: Experimental validation of total energy control system for uavs. Energies **13**(1) (2020). https://doi.org/10.3390/en13010014
11. Comer, A., Chakraborty, I.: Total energy-based control design and optimization for lift-plus-cruise aircraft. J. Guid. Control. Dyn. **47**(7), 1414–1436 (2024). https://doi.org/10.2514/1.G007605
12. Belokon, S.A., Zolotukhin, Y.N., Kotov, K.Y., Maltsev, A.S., Yan, A.P.: Artificial intelligence methods: total energy control of aircraft longitudinal motion. Optoelectron. Instrum. Data Process. **59**(5), 580–591 (2023). https://doi.org/10.3103/S8756699023050011
13. Stevens, B.L., Lewis, F.L.: Aircraft Control and Simulation. Wiley-Interscience, Hoboken, NJ, USA (2003)
14. Napolitano, M.R.: Aircraft Dynamics: From Modeling to Simulation. CourseSmart Series. Wiley, Hoboken, NJ, USA (2011)
15. Zipfel, P.H.: Modeling and Simulation of Aerospace Vehicle Dynamics. AIAA education series. American Institute of Aeronautics and Astronautics, Incorporated, Reston, VA, USA (2014)
16. De Marco, A., D'Onza, P., Manfredi, S.: A deep reinforcement learning control approach for high-performance aircraft. Nonlinear Dyn. **111**(18), 17037–17077 (2023). https://doi.org/10.1007/s11071-023-08725-y
17. U.S. Standard Atmosphere, 1976. National Oceanic and Atmospheric Administration, National Aeronautics and Space Administration, United States Air Force, Washington, D.C., USA (1976). NOAA-S/T 76-1562, NASA-TM-X-74335
18. Grazioso, G., Di Stasio, M., Nicolosi, F., Trepiccione, S.: A mathematical model for hybrid-electric propulsion system for regional propeller-driven aircraft. Energy Convers. Manag. X **26** (2025). https://doi.org/10.1016/j.ecmx.2025.100957
19. McCormick, B.W.: Aerodynamics, Aeronautics, and Flight Mechanics, 2nd edn. John Wiley & Sons, New York, USA (1995)
20. Stengel, R.F.: Flight Dynamics, 2nd edn. Princeton University Press, Princeton, NJ, USA (2022)
21. Molino, L., De Marco, A., Manfredi, S.: Energy-based multiple-input-multiple-output nonlinear control of fixed-wing aircraft. In: Advances in Nonlinear Dynamics. NODYCON Conference Proceedings Series. Springer, Gewerbestrasse 11, 6330 Cham, Switzerland (2026). https://doi.org/10.1007/978-3-032-16536-7_11
22. Ciliberti, D., De Marco, A., Terracciano, A., Borrelli, P.: Nonlinear control strategies in a co-simulation framework for hybrid regional aircraft design verification. In: Advances in Nonlinear Dynamics. NODYCON Conference Proceedings Series. Springer, Gewerbestrasse 11, 6330 Cham, Switzerland (2026). https://doi.org/10.1007/978-3-032-16536-7_13
23. Ciliberti, D., De Marco, A., Nicolosi, F.: Development and integration of a flight dynamics module into the ODE4HERA Open Digital Platform. Eng. Proc. **133**(1) (2026). https://doi.org/10.3390/engproc2026133063

Publisher's Note Springer Nature remains neutral with regard to jurisdictional claims in published maps and institutional affiliations.